ORIGINAL PAPER

Mixed unsplit-field perfectly matched layers for transient simulations of scalar waves in heterogeneous domains

Jun Won Kang · Loukas F. Kallivokas

Abstract We discuss a new formulation for transient scalar wave simulations in heterogeneous semi-infinite domains. To deal with the semi-infinite extent of the physical domains, we introduce truncation boundaries and adopt perfectly matched layers (PMLs) as the boundary wave absorbers. Within this framework, we develop a new mixed displacement-stress (or stress memory) finite element formulation based on unsplit-field PMLs. We use, as typically done, complex-coordinate stretching transformations in the frequency domain, and recover the governing partial differential equations in the time-domain through the inverse Fourier transform. Upon spatial discretization, the resulting equations lead to a mixed semi-discrete form, where both displacements and stresses (or stress histories/memories) are treated as independent unknowns. We propose approximant pairs, which, numerically, are shown to be stable. The resulting mixed finite element scheme is relatively simple and straightforward to implement, when compared against split-field PML techniques. It also bypasses the need for complicated time integration schemes that arise when recent displacement-based formulations are used. We report numerical results for 1D and 2D scalar wave propagation in semi-infinite domains truncated by PMLs. We also conduct parametric studies and report on the effect the various PML parameter choices have on the simulation error.

Keywords Unsplit-field perfectly matched layers (PMLs) · Mixed finite elements · Transient wave propagation · Semi-infinite domains

1 Introduction

The numerical simulation of wave motion is of importance in a variety of fields in science and engineering with, amongst others, significant applications in seismology, medicine, and geophysical probing. In such applications, it is often required to model the propagation of waves within domains that are mathematically idealized as unbounded, whether of infinite or semi-infinite extent. When domain discretization methods are used as the means to numerical solutions, especially in the presence of material heterogeneity, it is necessary that the unbounded domain be reduced to a finite one. This domain reduction is typically accomplished through a geometric truncation of the physical domain, accompanied by the prescription of appropriate boundary conditions on the truncation surface. Once the domain is truncated, there are two possible paths for dealing with propagating waves originating from the interior of the finite domain and impinging upon the artificial boundary: either allow their safe passage through the truncation surface with, ideally, no reflections from the artificial boundary, or enforce their vanishing while, again, ensuring that, at best, the wave motion in the interior domain is not adversely polluted. The former approach gives rise, mathematically, to *transparent conditions*, rightly termed for the sought benefit of

J. W. Kang · L. F. Kallivokas (✉)
Department of Civil, Architectural and Environmental Engineering, The University of Texas at Austin, 1 University Station, C1748, Austin, TX 78712, USA
e-mail: loukas@mail.utexas.edu

J. W. Kang
e-mail: jwkang@mail.utexas.edu

unimpeded wave propagation through the truncation surface. By contrast, the latter approach gives rise to *absorbing conditions*,[1] for waves are absorbed, usually within a buffer zone adjacent to the truncation surface.

There is a rich literature devoted to the development of transparent and absorbing boundary conditions, with early work dating back to the 1950s [1]. Whereas much has been done since, the problem in its most general form remains, by and large, open, whether one adopts transparent or absorbing conditions. Transparent conditions can be roughly classified into local and non-local, where the non-locality refers to the need for simultaneous spatial and temporal coupling at the truncation surface. That is, the response at every point on the artificial boundary is coupled with the *time histories* of the response at all other points along the boundary. Typically, such non-local conditions are exact and, thus, without reflections (in their continuous form), or truly transparent but difficult to construct and computationally onerous; they are only constructible for canonical geometries of the truncation surface (circular, spherical, ellipsoidal, rectangular, etc). However, when devising such non-local conditions, one typically assumes that the exterior domain, which is excluded from subsequent computations, is homogeneous [5, 6]. Such an assumption is quite restrictive since, in order to maintain consistency with the physical setting, it forces placement of the artificial boundary far from the region of interest, thus further exacerbating the computational cost. To date, there is no non-local condition devised that could account for arbitrary heterogeneity, nor is it presently conceivable that such a condition is possible to construct. It should be emphasized that, by construction, the perfectly matched layer (PML) allows for arbitrary heterogeneity within the computational domain but cannot, also by construction, account for exterior heterogeneity (information does not travel beyond the PML, nor is any information from the exterior brought to bare on the PML's construction). A notable exception to the need for exterior homogeneity is the so called pole condition, introduced by Schmidt [2–4]. The pole condition is used to construct transparent conditions valid for exterior heterogeneous domains, which, however, have to be piecewise homogeneous, characterized by constant wavenumbers on a per-segment basis. Though there is some built-in flexibility, the approach has thus far been implemented in the frequency domain only, and it is difficult to see how it can be generalized to arbitrarily heterogeneous domains.

By contrast to non-local transparent conditions, local conditions aim at relaxing either the temporal or the spatial non-locality or both, in an attempt to ease the computational cost, but also to lend much needed generality [7–11]. Relaxations of the non-locality, however, come at the expense of transparency, since they introduce non-physical reflections that typically pollute the solution in the interior domain. They are capable of better addressing structured heterogeneity (e.g., moduli with a simple functional dependence on space) than non-local conditions, but proper treatment of arbitrary heterogeneity remains elusive.

Alternatively, the wave motion could be dampened or, even better, artificially killed, once it reaches (or passes) the truncation surface, and, ideally, without generating any reflections from it. The concept was central to the so-called sponge layers, first proposed by Israeli and Orszag in 1981 [19], but the resulting scheme introduced reflections at the interface. Since then, much of the development focused on transparency conditions, until 1994, when the absorption concept re-emerged following Bérenger's introduction of the PMLs in the context of electromagnetics [12]. The PMLs are designed to attenuate the waves within a relatively small buffer zone (the layers) surrounding the regular (physical) domain, while at the same time perfectly matching the impedances between the regular and PML domains at the truncation surface. The impedance matching implies that reflections are eliminated for all incidence angles and frequencies. While the construction of the PMLs depends on the geometry of the truncation surface, the dependence is not as onerous as it is in the case of transparent conditions, for which the spatial non-locality drives complexity. More importantly though, the PMLs are capable of accommodating heterogeneity—a key shortcoming of the majority of other developments.

Since Bérenger's introduction of the PMLs, much has been done, and the concept was used not only in electromagnetics, but in acoustics and elastodynamics as well. For example, Hu [14] and Hesthaven [15] explored the application of the split-field PMLs for linearized Euler equations, while Harari et al. [16, 17] and Turkel [18] formulated the PMLs for the Helmholtz equation. Qi and Geers [20] also used the PMLs for acoustics, and Zeng et al. [21] formulated the PMLs for poroelasticity.

Early on, implementations of the PML generally followed either of two paths: split-field or unsplit-field formulations, where the former refers to the partitioning of the motion in components, and the latter simply

---

[1]In the literature, the terms absorbing, artificial, silent, transparent, truncating, etc., have often been used interchangeably to describe the boundary conditions imposed on the artificial boundary. Here, we try to adhere to a terminology consistent with the physical implications of the mathematical conditions.

juxtaposes the former. For example, in two dimensions, and for straight truncation boundaries, the split-field formulation partitions the total wavefield into a component parallel and a component vertical to the truncation boundary. In 1994, Chew and Weedon re-interpreted Bérenger's initial idea in terms of a complex-coordinate stretching procedure [13]. The authors first split the wavefield and then enforced the coordinate stretching only to the wavefield component perpendicular to the regular domain–PML interface, thus giving rise to a split-field formulation.

In elastodynamics, Chew and Liu [22] also used complex-coordinate stretching ideas. They formulated a velocity-stress split-field PML, and used a finite difference time domain (FDTD) scheme for the numerical implementation. Following their work, Hastings et al. developed a PML scheme for elastic waves in terms of the P- and S-wave potentials [23]. Collino and Monk [25] formulated PMLs for general curvilinear coordinates, and in 1999, Liu [24] discussed PMLs for elastodynamics in cylindrical and spherical coordinates.

In [26], Collino and Tsogka discussed a velocity-stress split-field PML using mixed finite elements in anisotropic heterogeneous media in the context of an FDTD formulation. Later, anisotropic PMLs for elastic waves were systematically explored in cartesian and curvilinear coordinates by Zheng and Huang [27] using an unsplit-field scheme. Despite the otherwise excellent performance of PMLs even in the presence of anisotropy and heterogeneity, there still remain open issues, with the chief amongst them the stability of the PMLs in transient applications (e.g., see [28] for the split-field PMLs, and [29, 30] for anisotropic cases). From an implementation point of view, the finite difference method (FDM) has been dominant, owing to the origins of the method in electromagnetics where FDM remains the numerical method of choice, but finite elements, and, more recently, spectral element implementations, have also appeared [31].

We remark that most of the aforementioned developments are based on split-field formulations, which typically require additional variables and are harder to implement directly using classic Galerkin-type finite element approaches. On the other hand, unsplit-field PMLs, for which no additional variables need to be introduced, have mostly appeared in frequency-domain implementations. This is so for good reason, as inversion back in the time-domain of the frequency-domain PML equations gives rise to higher-order time derivatives, which, in turn, lead to formulations that depart from the second-order forms typical (and familiar) of displacement-based elastodynamics.

A notable exception is the work of Basu and Chopra [32, 33], who adopted a displacement-based finite element scheme to implement unsplit-field PML equations directly in the time-domain. However, their formulation results in a complicated scheme for the temporal integration of the semi-discrete forms. To overcome these difficulties, we discuss here a new formulation that hinges on a mixed method, where both displacements and stresses are treated as unknowns. Our motivation does not stem from a desire to fill an apparent gap in the array of PML-based formulations developed to date, but rather from a need to provide a methodology that leads to a scheme that could be easily implemented whether one uses it for forward or for *inverse* problems, where adjoint-type approaches stand to benefit from a simple formulation. In fact, this work was initiated because of the lack of forward schemes that can readily be used in adjoint formulations arising in inverse problems.

We remark that most PML developments to date, including the one we discuss herein, lead to mixed formulations. In addition, most developments rely on split-field mixed formulations, where all the components of the displacement (or velocity) field and the stress field are treated as unknowns. In most cases, the numerical scheme of choice has been finite differences. Thus, implementations of the resulting mixed strong forms using finite elements have received little attention. There are a handful of exceptions, and in order to place our development in context, we next briefly discuss developments related to mixed methods; a comprehensive review is well outside the scope of this article, but an outstanding discussion has been provided by Arnold in [39].

In a survey of mixed finite element methods by Brezzi in [40], the author pointed out that there exist two possible variational forms for treating a mixed problem such as the one arising in elasticity (the author discussed the formulations in the context of a Poisson-type problem, but the conclusions are more general). The two forms result in *decidedly different* regularity requirements for the approximants. In the first form, the regularity required for the stress approximants is higher than that of the displacement approximants; this is the classic mixed method, which requires highly specialized elements. A first family of mixed finite elements related to this variational form was introduced by Raviart and Thomas for second-order elliptic problems (RT elements) [41], followed later on by several others (see, e.g., [42–45], etc). Other related developments can be found in [34–36, 46–61]. It should be noted that: (a) these specialized elements typically require a high number of degrees of freedom, which are associated not

only with nodal quantities, but also with edge quantities (normal derivatives), and (b) the stability of the elements that are consistent with this first variational form is still an open problem in elasticity.

On the other hand, in a second variational form, which differs from the first simply by an integration by parts, the regularity requirements are somewhat reversed: the regularity for the displacement approximants should be higher than that of the stress approximants. The latter requirements are less onerous for implementation purposes and do not require any special element types. In this work, we favor this second, and largely unexplored, variational form.

To date, there are four developments that are closely related to ours, but they all differ in substantial ways: Bécache et al. in [55] used a classic mixed method, but split fields; Cohen and Fauqueux [63] used a unique mixed method, unlike any other in the literature, where they use the displacement vector, the displacement gradients (not the strain tensor), and the components of a stress-like tensor as unknowns; Festa and Vilotte [62] use the same non-classic mixed method as ours, but end up using split-fields; and finally, Basu and Chopra [32] came close to casting the problem in a mixed form using unsplit fields in a manner similar to ours, but ended up with a discrete implementation that destroyed the mixed form, in favor of a complicated time-marching scheme.

Thus, by contrast to other prior developments, in this article, we discuss a new displacement-stress, or more precisely, stress-memory or stress-history, mixed finite element formulation that allows the direct temporal integration of the semi-discrete forms resulting from unsplit-field PML equations. This is accomplished at the expense of symmetry of the resulting semi-discrete forms, but is shown to retain the second-order temporal character, with its associated implementational ease.

We discuss numerical experiments in one and two dimensions using scalar waves involving both homogeneous and heterogeneous domains, and numerically study the effect various PML parameters have on the simulation error.

2 One-dimensional unsplit-field PML

2.1 Complex coordinate stretching

To fix ideas and be able to place the formulation we propose in context, we repeat here the basic steps leading to the PML-augmented equations, cast directly in the time-domain: the origins can be traced to the works we referred to in the preceding section. In
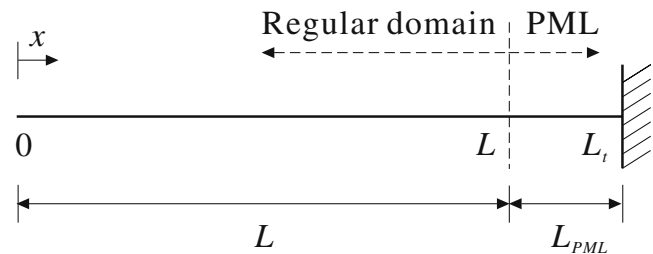

Fig. 1 A PML-truncated semi-infinite domain in one dimension

one dimension, the time-harmonic, viscously damped wave motion is governed by the following equation of equilibrium, constitutive law, and kinematic condition, respectively:

$$\frac{d\hat{\sigma}}{dx} = -\omega^2 \rho \hat{u} + i\omega\beta\hat{u}, \tag{1a}$$

$$\hat{\sigma} = E\hat{\epsilon}, \tag{1b}$$

$$\hat{\epsilon} = \frac{d\hat{u}}{dx}, \tag{1c}$$

where ρ is mass density, E is Young's modulus, u denotes displacement, σ denotes stress, ϵ denotes strain, ω is circular frequency, and i is the imaginary unit. The functions $\hat{u}$, $\hat{\sigma}$, and $\hat{\epsilon}$ depend on x and the frequency ω, and a caret (ˆ) denotes the Fourier transform of the subtended function. The viscous damping parameter β is included here in order to account for simple material damping; the physical setting of the applicability of Eq. 1 includes layered soils, cables, and rods.

Following classical lines, to solve the system of equations in Eq. 1 within a semi-infinite domain, where $0 \le x < \infty$, we truncate the semi-infinite extent of the domain at $x = L$, attach a PML of finite length L_{PML} to the now finite computational domain of interest, and force the attenuation of the outgoing waves within this relatively small buffer zone L_{PML}. Figure 1 depicts the (truncated) computational or regular domain, which is extended by the PML.

To enforce wave attenuation within the PML, we recast Eq. 1 by "stretching" the real coordinate x to $\tilde{x}$, using the map [13]:

$$\tilde{x} = \int_0^x \lambda(s)ds = \int_0^x \left(1 - i\frac{f(s)}{a_0}\right)ds = x - \frac{i}{a_0}\int_0^x f(s)ds, \tag{2}$$

in which $a_0(= kb)$ is a dimensionless frequency, with b being a characteristic length of the domain of interest.[2]

---

[2]The characteristic length b will eventually cancel out of the subsequently developed equations.

In Eq. 2, $f(x)$ is an attenuation function defined over the entire domain ($L_t = L + L_{PML}$), such that $f(x) \equiv 0$ within the regular domain ($0 \leq x \leq L$), and $f(x) > 0$ within the PML ($L < x \leq L_t$) ($f(x)$ satisfies continuity at the regular domain–PML interface). With this in mind, $\tilde{x} \equiv x$ within the regular domain ($0 \leq x \leq L$), and Eq. 2 can be rewritten as:

$$\tilde{x} = x - i\frac{F(x)}{a_0}, \qquad \text{where} \quad F(x) := \int_0^x f(s)ds. \quad (3)$$

Provided that $F(x) > 0$, it can be easily seen that an outgoing wave satisfying the system of equations in Eq. 1 decays exponentially within the PML domain since[3]

$$u(\tilde{x}) = \exp\left[-ik\tilde{x}\right] = \exp\left[-\frac{F(x)}{b}\right]\exp\left[-ikx\right]. \quad (4)$$

The exponential decay does not depend on frequency, as suggested by the frequency-independent amplitude in Eq. 4. Furthermore, the interface "perfectly matches" the outgoing motion, i.e., it does not reflect propagating waves for all frequencies [12, 22, 26].

2.2 Determination of the wave attenuation function $f(x)$

From Eq. 4, it is clear that $f(x)$ plays a central role in imposing wave attenuation within the PML. There is no absolute criterion, nor has one been suggested, in determining the precise form of the attenuation function; here, we try to derive it based on physical grounds. Specifically, a time-harmonic wave motion in the PML can be represented as the summation of a propagating wave and the reflected wave from the fixed boundary at $x = L_t$; assuming unity for the amplitude of the propagating wave, there results

$$\hat{u}(x) = \exp\left(-ik\tilde{x}\right) + R\exp\left(ik\tilde{x}\right), \qquad L \leq x \leq L_t, \quad (5)$$

where R is a (complex) reflection coefficient. Substituting Eq. 3 into Eq. 5, and imposing the boundary condition $u(L_t) = 0$, there results

$$|R| = \exp\left[-\frac{2F(L_t)}{b}\right]. \quad (6)$$

In order to obtain $F(L_t)$, we assume a polynomial form for $f(x)$:

$$f(x) = \begin{cases} 0, & 0 \leq x \leq L, \\ f_0\left(\frac{x-L}{L_{PML}}\right)^m, & L \leq x \leq L_t, \end{cases} \quad (7)$$

where f_0 is a parameter to be determined, and m is the polynomial order of the attenuation function. Then, use of the definition Eq. 3 results in:

$$F(L_t) = \int_0^{L_t} f(s)ds = \int_L^{L_t} f_0\left(\frac{s-L}{L_{PML}}\right)^m ds = \frac{f_0 L_{PML}}{m+1}. \quad (8)$$

Therefore, using Eqs. 6 and 8, $|R|$ can be written as:

$$|R| = \exp\left[-\frac{2f_0 L_{PML}}{b(m+1)}\right]. \quad (9)$$

As also discussed by Basu and Chopra in [33], the reflection coefficient $|R|$ is inversely proportional to f_0 or L_{PML}. That is, $|R|$ decreases when f_0 or L_{PML} increases. f_0 in Eq. 7 remains to be determined. Instead of choosing an arbitrary large number for f_0, we express it in terms of $|R|$, L_{PML}, m, and b from Eq. 9 as follows:

$$f_0 = \frac{(m+1)b}{2L_{PML}}\log\left(\frac{1}{|R|}\right). \quad (10)$$

For example, if the attenuation function $f(x)$ is chosen to be of second order ($m = 2$), then:

$$f(x) = \frac{3b}{2L_{PML}}\log\left(\frac{1}{|R|}\right)\left(\frac{x-L}{L_{PML}}\right)^2, \quad (11)$$

where $|R|$ is now a *user-tunable* parameter that controls the amount of reflection from the fixed boundary at $x = L_t$, as well as the strength of the attenuation within the PML (by virtue of Eq. 11). In applications, we favor the quadratic form of $f(x)$ over other orders due to the gradual and smooth wave decay that it enforces within the PML; the form has been widely used [26, 27, 31].

2.3 Mixed form of the transient PML equations

In Eq. 2, the complex coordinate stretching function $\lambda(x)$ was introduced as:

$$\lambda(x) = 1 - i\frac{f(x)}{a_0} = 1 - i\frac{g(x)}{k}, \quad (12)$$

where

$$g(x) = \frac{1}{b}f(x), \quad (13)$$

---

[3]Here, for simplicity, we consider $\beta = 0$. A harmonic factor $e^{i\omega t}$ has been considered throughout.

is the normalized attenuation function. Differentiating Eq. 2 with respect to x yields the following differential operator:

$$\frac{d}{d\tilde{x}} = \frac{1}{\lambda(x)} \frac{d}{dx}. \tag{14}$$

Next, we rewrite the system of equations in Eq. 1 using the stretched coordinate $\tilde{x}$, i.e., we replace x with $\tilde{x}$ in Eq. 1, while also using Eq. 14. There results:

$$\frac{1}{\lambda(x)} \frac{d\hat{\sigma}}{dx} = -\omega^2 \rho \hat{u} + i\omega\beta \hat{u}, \tag{15a}$$

$$\hat{\sigma} = E\hat{\epsilon}, \tag{15b}$$

$$\hat{\epsilon} = \frac{1}{\lambda(x)} \frac{d\hat{u}}{dx}. \tag{15c}$$

Multiplying by $\lambda(x)$ both sides of Eq. 15a, while considering Eq. 12, results in:

$$\frac{d\hat{\sigma}}{dx} = -\omega^2 \rho \left(1 - i\frac{g(x)}{k}\right) \hat{u} + i\omega\beta \left(1 - i\frac{g(x)}{k}\right) \hat{u}$$

$$= -\omega^2 \rho \hat{u} + i\omega \left(\rho cg + \beta\right) \hat{u} + \beta cg\hat{u}. \tag{16}$$

Next, multiplying with $i\omega\lambda(x)$ both sides of Eq. 15c yields:

$$i\omega \left(1 - i\frac{g(x)}{k}\right) \hat{\epsilon} = i\omega \frac{d\hat{u}}{dx}, \quad \text{or}$$

$$i\omega\hat{\epsilon} + cg\hat{\epsilon} = i\omega \frac{d\hat{u}}{dx}. \tag{17}$$

Equations 16, 15b, and 17 are next inverted back to the time-domain to yield:

$$\frac{\partial\sigma}{\partial x} = \rho \frac{\partial^2 u}{\partial t^2} + (\rho cg + \beta) \frac{\partial u}{\partial t} + \beta cg u, \tag{18a}$$

$$\sigma = E\epsilon, \tag{18b}$$

$$\frac{\partial\epsilon}{\partial t} + cg\epsilon = \frac{\partial^2 u}{\partial x \partial t}, \tag{18c}$$

in which $c = \sqrt{(E/\rho)}$ is the wave velocity. The modified constitutive and compatibility equations (Eqs. 18b and 18c) can be combined together to yield:

$$\frac{\partial\sigma}{\partial t} + cg\sigma = \rho c^2 \frac{\partial^2 u}{\partial x \partial t}. \tag{19}$$

Next, we normalize the displacement and viscous damping with respect to the density, i.e., we set $v = \rho u$ and $\zeta = \beta/\rho$ and recast Eqs. 18a and 19 as:

$$\frac{\partial^2 v}{\partial t^2} + (cg + \zeta) \frac{\partial v}{\partial t} + \zeta cg v - \frac{\partial\sigma}{\partial x} = 0, \tag{20a}$$

$$\frac{\partial\sigma}{\partial t} + cg\sigma - c^2 \frac{\partial^2 v}{\partial x \partial t} = 0. \tag{20b}$$

Equation 20 is the displacement(v)-stress(σ) mixed equation governing transient wave propagation in a PML-truncated one-dimensional domain. Notice that the PML-enhanced equations (Eq. 20) are still second-order in time.

3 Unsplit-field PML for SH waves

The above procedure can be similarly applied to obtain the unsplit-field mixed PML equations for scalar waves (SH) in two dimensions. The development is based on cartesian coordinates.

3.1 Two-dimensional complex coordinate stretching

The equations governing anti-plane motion in the frequency domain are:

$$\nabla \cdot \hat{\boldsymbol{\sigma}} = -\omega^2 \rho \hat{u}, \tag{21a}$$

$$\hat{\boldsymbol{\sigma}} = 2\mu\hat{\boldsymbol{\epsilon}}, \tag{21b}$$

$$\hat{\boldsymbol{\epsilon}} = \frac{1}{2}\nabla\hat{u}, \tag{21c}$$

where

$$\boldsymbol{\sigma} = [\sigma_{31} \ \sigma_{32}]^{\mathrm{T}}, \tag{22a}$$

$$\boldsymbol{\epsilon} = [\epsilon_{31} \ \epsilon_{32}]^{\mathrm{T}}, \tag{22b}$$

$$\nabla u = \left[\frac{\partial u}{\partial x_1} \ \frac{\partial u}{\partial x_2}\right]^{\mathrm{T}}, \tag{22c}$$

in which μ denotes the shear modulus of the medium; x_1 and x_2 are cartesian planar coordinates (Fig. 2); and indices 1, 2, and 3 indicate components along the x_1, x_2, and x_3 axes, respectively, with x_3 denoting the antiplane axis.

We introduce complex coordinate stretching in each of x_1 and x_2 in order to rewrite the governing equations for the combined regular domain–PML region as shown in Fig. 2. The corresponding coordinate stretching functions $\lambda_1(x_1)$ and $\lambda_2(x_2)$ are defined as:

$$\lambda_j(x_j) = \left\{1 + f_j^e(x_j)\right\} - i\frac{f_j^p(x_j)}{a_0}, \quad j = 1, 2, \tag{23}$$

where f_j^e $(j = 1, 2)$ are attenuation functions for evanescent waves, and $f_j^p(j = 1, 2)$ are attenuation functions for propagating waves in each j direction. $a_0(= kb)$ denotes again dimensionless frequency, and b is a characteristic length of the system. Notice that $\lambda_1(x_1)$ and $\lambda_2(x_2)$ depend on x_1 and x_2, respectively.
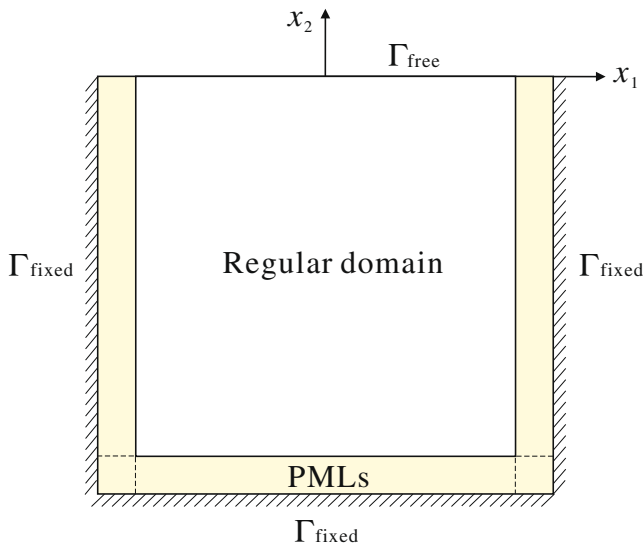
Fig. 2 A PML-truncated semi-infinite domain in two dimensions

Next, we introduce the stretched coordinates $\tilde{x}_1$ and $\tilde{x}_2$, defined as:

$$\tilde{x}_j = \int_0^{x_j} \lambda_j(s)\,ds = \int_0^{x_j} \left[\left\{ 1 + f_j^e(s) \right\} - i\frac{f_j^p(s)}{a_0} \right] ds,$$

$$j = 1, 2. \tag{24}$$

Then, plane propagating waves $(\hat{u}_p)$ and evanescent waves $(\hat{u}_e)$ that satisfy Eq. 21 can be written using the stretched coordinates $\tilde{\mathbf{x}}$ as:

$$\hat{u}_p(\tilde{\mathbf{x}}) = \exp\left[-ik\tilde{\mathbf{x}} \cdot \mathbf{d} \right]$$

$$= \exp\left[-\frac{1}{b} \left(F_1^p d_1 + F_2^p d_2 \right) \right]$$

$$\times \exp\left[-ik \left(F_1^e d_1 + F_2^e d_2 \right) \right]$$

$$\times \exp\left[-ik\mathbf{x} \cdot \mathbf{d} \right], \tag{25}$$

$$\hat{u}_e(\tilde{\mathbf{x}}) = -\exp\left[-k\tilde{\mathbf{x}} \cdot \mathbf{d} \right]$$

$$= -\exp\left[-k \left(F_1^e d_1 + F_2^e d_2 \right) \right]$$

$$\times \exp\left[i\frac{1}{b} \left(F_1^p d_1 + F_2^p d_2 \right) \right]$$

$$\times \exp\left[-k\mathbf{x} \cdot \mathbf{d} \right], \tag{26}$$

where F_j^e and F_j^p are obtained by integrating f_j^e and f_j^p from 0 to x_j ($j = 1, 2$), respectively. $\mathbf{d} = \begin{bmatrix} d_1 & d_2 \end{bmatrix}^{\mathrm{T}}$ denotes the direction of wave propagation. Equation 25 suggests that a plane scalar wave propagating in a direction $\mathbf{d}$ decays exponentially within the PML, provided that $F_1^p d_1 + F_2^p d_2 > 0$. Similarly, an evanescent wave experiences attenuation within the PML, provided that

$F_1^e d_1 + F_2^e d_2 > 0$. Whereas the attenuation of evanescent waves depends on frequency, the attenuation of propagating waves does not. Since the stretched coordinate $\tilde{x}$ and the original coordinate x match at the interface between the regular domain and the PML, the interface does not reflect outgoing waves for any frequency and any angle of incidence (in the continuous form).

3.2 Mixed form of the transient PML equations for SH waves

We modify the equation of motion Eq. 21a by writing it again in the stretched coordinates $\tilde{\mathbf{x}}$ defined by Eq. 24. That is, we replace x_j with $\tilde{x}_j$ and rewrite Eq. 21a as:

$$\frac{1}{\lambda_1} \frac{\partial \hat{\sigma}_{31}}{\partial x_1} + \frac{1}{\lambda_2} \frac{\partial \hat{\sigma}_{32}}{\partial x_2} = -\omega^2 \rho \hat{u}, \tag{27}$$

where we used the following differential operators:

$$\frac{\partial}{\partial \tilde{x}_j} = \frac{1}{\lambda_j} \frac{\partial}{\partial x_j}, \qquad j = 1, 2, \tag{28}$$

which, in turn, are derived by differentiating Eq. 24 with respect to x_j, just as we did in the one-dimensional case. Next, multiplying by $\lambda_1\lambda_2$ both sides of Eq. 27 and recalling that λ_1 is a function of x_1, and λ_2 is a function of x_2, Eq. 27 is modified to read:

$$\nabla \cdot \left(\tilde{\Lambda}\hat{\sigma} \right) = -\omega^2 \rho \lambda_1 \lambda_2 \hat{u}. \tag{29}$$

In [32], Basu and Chopra defined the stretch tensor $\tilde{\Lambda}$ as:

$$\tilde{\Lambda} = \begin{bmatrix} \lambda_2 & 0 \\ 0 & \lambda_1 \end{bmatrix} = \tilde{\mathbf{F}}^e + \frac{1}{i\omega}\tilde{\mathbf{F}}^p, \tag{30}$$

where

$$\tilde{\mathbf{F}}^e = \begin{bmatrix} 1 + f_2^e & 0 \\ 0 & 1 + f_1^e \end{bmatrix}, \qquad \tilde{\mathbf{F}}^p = \begin{bmatrix} c_s g_2^p & 0 \\ 0 & c_s g_1^p \end{bmatrix}, \tag{31}$$

and c_s denotes shear wave velocity, i.e., $c_s = \sqrt{\mu/\rho}$; and $g_i^p = f_i^p/b$ are normalized attenuation functions with respect to b. We apply the inverse Fourier transform to Eq. 29 to obtain the corresponding equation in the time domain, replacing λ_1 and λ_2 with the right-hand terms of Eq. 23. There results:

$$\nabla \cdot \left(\tilde{\mathbf{F}}^e \boldsymbol{\sigma} + \tilde{\mathbf{F}}^p \int_0^t \boldsymbol{\sigma}(\mathbf{x}, \tau)\,d\tau \right) = \rho f_m \ddot{u} + \rho c_s g_c \dot{u} + \mu g_k u, \tag{32}$$

where

$$f_m = \left(1 + f_1^e\right)\left(1 + f_2^e\right), \tag{33a}$$

$$g_c = g_2^p\left(1 + f_1^e\right) + g_1^p\left(1 + f_2^e\right), \tag{33b}$$

$$g_k = g_1^p g_2^p. \tag{33c}$$

Equation 21c is similarly inverted back to the time-domain using the same procedure as above. Specifically, introduction of the stretched coordinates in the kinematic conditions results in:

$$\hat{\boldsymbol{\epsilon}} = \frac{1}{2}\Lambda\nabla\hat{u}, \tag{34}$$

in which, by borrowing the notation from [32], the stretch tensor Λ is defined as:

$$\Lambda = \begin{bmatrix} \frac{1}{\lambda_1} & 0 \\ 0 & \frac{1}{\lambda_2} \end{bmatrix} = \left[\mathbf{F}^e + \frac{1}{i\omega}\mathbf{F}^p\right]^{-1}, \tag{35}$$

where

$$\mathbf{F}^e = \begin{bmatrix} 1 + f_1^e & 0 \\ 0 & 1 + f_2^e \end{bmatrix}, \qquad \mathbf{F}^p = \begin{bmatrix} c_s g_1^p & 0 \\ 0 & c_s g_2^p \end{bmatrix}. \tag{36}$$

Pre-multiplying both sides of Eq. 34 by $i\omega\Lambda^{-1}$, and inverting it back to the time-domain, results in:

$$\mathbf{F}^e\dot{\boldsymbol{\epsilon}} + \mathbf{F}^p\boldsymbol{\epsilon} = \frac{1}{2}\nabla\dot{u}. \tag{37}$$

Now, Eq. 21 has its counterpart in the time domain as:

$$\nabla\cdot\left(\tilde{\mathbf{F}}^e\boldsymbol{\sigma} + \tilde{\mathbf{F}}^p\int_0^t\boldsymbol{\sigma}(\mathbf{x},\tau)d\tau\right) = \rho f_m\ddot{u} + \rho c_s g_c\dot{u} + \mu g_k u, \tag{38a}$$

$$\boldsymbol{\sigma} = 2\mu\boldsymbol{\epsilon}, \tag{38b}$$

$$\mathbf{F}^e\dot{\boldsymbol{\epsilon}} + \mathbf{F}^p\boldsymbol{\epsilon} = \frac{1}{2}\nabla\dot{u}. \tag{38c}$$

Equations 38b and 38c can be combined together to yield:

$$\mathbf{F}^e\dot{\boldsymbol{\sigma}} + \mathbf{F}^p\boldsymbol{\sigma} = \mu\nabla\dot{u}. \tag{39}$$

Up to this point, the development parallels that of others, most notably [32]. Our point of departure is the treatment of Eq. 38a, which includes a term that requires the temporal integration of stress, i.e., $\int_0^t\boldsymbol{\sigma}(\mathbf{x},\tau)d\tau$, which, in turn, requires the storage of the stress history. We introduce:

$$\mathbf{s}(\mathbf{x},t) = \int_0^t\boldsymbol{\sigma}(\mathbf{x},\tau)d\tau, \qquad \mathbf{s} = [s_1\ s_2]^T, \tag{40}$$

such that

$$\dot{\mathbf{s}}(\mathbf{x},t) = \boldsymbol{\sigma}(\mathbf{x},t), \tag{41a}$$

$$\ddot{\mathbf{s}}(\mathbf{x},t) = \dot{\boldsymbol{\sigma}}(\mathbf{x},t). \tag{41b}$$

By substituting Eqs. 40 and 41 into Eqs. 38a and 39, while setting again $v = \rho u$, we obtain a displacement (v)–stress memory[4] mixed form of the equations governing the propagation of SH waves:

$$f_m\ddot{v} + c_s g_c\dot{v} + c_s^2 g_k v - \nabla\cdot\left(\tilde{\mathbf{F}}^e\dot{\mathbf{s}} + \tilde{\mathbf{F}}^p\mathbf{s}\right) = 0, \tag{42a}$$

$$\mathbf{F}^e\ddot{\mathbf{s}} + \mathbf{F}^p\dot{\mathbf{s}} - c_s^2\nabla\dot{v} = 0. \tag{42b}$$

4 Mixed finite element implementation

4.1 One-dimensional mixed FE-formulation

Equations 20 include both displacements (v) and stresses (σ). To obtain approximate solutions, we employ a mixed finite element scheme [37, 38, 40]. The associated initial-boundary-value problem (IBVP) in the PML-truncated semi-infinite domain becomes:

$$\frac{\partial^2 v}{\partial t^2} + (cg + \zeta)\frac{\partial v}{\partial t} + \zeta cg v - \frac{\partial\sigma}{\partial x} = 0, \tag{43a}$$

$$\frac{\partial\sigma}{\partial t} + cg\sigma - c^2\frac{\partial^2 v}{\partial x\partial t} = 0, \tag{43b}$$

$$\text{for } x \in (0,\ L_t)\ ,\ t \in (0,\ T],$$

$$v(L_t, t) = 0, \tag{44a}$$

$$\sigma(0, t) = p(t), \tag{44b}$$

$$v(x, 0) = 0, \tag{44c}$$

$$\dot{v}(x, 0) = 0, \tag{44d}$$

$$\sigma(x, 0) = 0. \tag{44e}$$

For the mixed finite element implementation of the IBVP given by Eqs. 43 and 44, both v and σ are treated as independent variables that need to be approximated separately. We remark that there are two possible variational forms derivable from the IBVP Eq. 43: in the first variational form only the last term in Eq. 43a is integrated by parts. In a second possible variational form, it is only the last term in Eq. 43b that is integrated by parts. The resulting two forms differ decidedly in the smoothness requirements they impose on the test and trial functions, with the former requiring less regularity on the stresses than the latter. For this reason alone, in this work we opt for the first variational form: accordingly, we seek $v \simeq v_h \in H^h \subset H_0^1(\Omega)$ and $\sigma \simeq$

---

[4]We use the term "stress memory" for $\mathbf{s}$ to differentiate from its right-hand side, which includes the explicit computation of the stress history; they are otherwise equivalent.

$\sigma_h \in Q^h \subset L^2(\Omega)$ such that Eq. 43 is satisfied. Next, we multiply Eqs. 43a and 43b by appropriate test functions $w(x)$ and $q(x)$, and then integrate over the entire domain $(0, L_t)$ in order to arrive at the corresponding weak forms:

$$\int_0^{L_t} w \left\{ \frac{\partial^2 v}{\partial t^2} + (cg + \zeta) \frac{\partial v}{\partial t} + \zeta cg v \right\} dx$$

$$+ \int_0^{L_t} \frac{dw}{dx} \sigma \, dx = -w(0) p(t), \qquad (45a)$$

$$- \int_0^{L_t} c^2 q \frac{\partial^2 v}{\partial x \partial t} dx$$

$$+ \int_0^{L_t} q \frac{\partial \sigma}{\partial t} dx + \int_0^{L_t} cg q \sigma \, dx = 0. \qquad (45b)$$

In Eq. 45, v and σ are approximated as:

$$v(x, t) \simeq \boldsymbol{\phi}(x)^{\mathrm{T}} \mathbf{v}(t), \qquad \sigma(x, t) \simeq \boldsymbol{\psi}(x)^{\mathrm{T}} \boldsymbol{\sigma}(t), \qquad (46)$$

where $\boldsymbol{\phi}$ and $\boldsymbol{\psi}$ are vectors of approximants associated with nodal displacements $\mathbf{v}(= \rho \mathbf{u})$ and nodal stresses $\boldsymbol{\sigma}$, respectively. The two test functions $w(x)$ and $q(x)$ are similarly approximated by the same approximants $\boldsymbol{\phi}$ and $\boldsymbol{\psi}$, respectively, i.e.,

$$w(x) \simeq \mathbf{w}^{\mathrm{T}} \boldsymbol{\phi}(x), \qquad q(x) \simeq \mathbf{q}^{\mathrm{T}} \boldsymbol{\psi}(x). \qquad (47)$$

To ensure solution stability, the choice of the approximants $\boldsymbol{\phi}$ and $\boldsymbol{\psi}$ cannot be arbitrary [37, 38]; here, we opted for piecewise linear basis functions $\boldsymbol{\phi}$ and piecewise constant basis functions $\boldsymbol{\psi}$, which *numerically* have been seen to satisfy the LBB condition. Introducing the approximants in Eq. 45 results in the following semi-discrete form:

$$\begin{bmatrix} \int_0^{L_t} \boldsymbol{\phi} \boldsymbol{\phi}^{\mathrm{T}} dx & \mathbf{0} \\ \mathbf{0} & \mathbf{0} \end{bmatrix} \begin{bmatrix} \ddot{\mathbf{v}} \\ \ddot{\boldsymbol{\sigma}} \end{bmatrix}$$

$$+ \begin{bmatrix} \int_0^{L_t} (cg + \zeta) \boldsymbol{\phi} \boldsymbol{\phi}^{\mathrm{T}} dx & \mathbf{0} \\ - \int_0^{L_t} c^2 \boldsymbol{\psi} \boldsymbol{\phi}'^{\mathrm{T}} dx & \int_0^{L_t} \boldsymbol{\psi} \boldsymbol{\psi}^{\mathrm{T}} dx \end{bmatrix} \begin{bmatrix} \dot{\mathbf{v}} \\ \dot{\boldsymbol{\sigma}} \end{bmatrix}$$

$$+ \begin{bmatrix} \int_0^{L_t} \zeta cg \boldsymbol{\phi} \boldsymbol{\phi}^{\mathrm{T}} dx & \int_0^{L_t} \boldsymbol{\phi}' \boldsymbol{\psi}^{\mathrm{T}} dx \\ \mathbf{0} & \int_0^{L_t} cg \boldsymbol{\psi} \boldsymbol{\psi}^{\mathrm{T}} dx \end{bmatrix} \begin{bmatrix} \mathbf{v} \\ \boldsymbol{\sigma} \end{bmatrix}$$

$$= \begin{bmatrix} (w\sigma)\big|_0^{L_t} \\ \mathbf{0} \end{bmatrix}. \qquad (48)$$

4.2 Two-dimensional mixed FE-formulation

We adopt again a mixed finite element method instead of a displacement-based finite element approach, by considering v, s_1, and s_2 as independent unknowns. The associated IBVP for SH waves in the two-dimensional PML-truncated semi-infinite domain can be stated as follows:

$$f_m \ddot{v} + c_s g_c \dot{v} + c_s^2 g_k v - \nabla \cdot \left(\tilde{\mathbf{F}}^e \dot{\mathbf{s}} + \tilde{\mathbf{F}}^p \mathbf{s} \right) = 0, \qquad (49a)$$

$$\mathbf{F}^e \ddot{\mathbf{s}} + \mathbf{F}^p \dot{\mathbf{s}} - c_s^2 \nabla \dot{v} = 0, \qquad (49b)$$

$$\text{in } \Omega \times (0, T],$$

$$v(\mathbf{x}, t) = 0 \qquad \text{on } \Gamma_{\text{fixed}} \times (0, T], \qquad (50a)$$

$$\dot{s}_2(\mathbf{x}, t) = p(\mathbf{x}, t) \qquad \text{on } \Gamma_{\text{free}} \times (0, T], \qquad (50b)$$

$$v(\mathbf{x}, 0) = 0 \qquad \text{on } \Omega, \qquad (50c)$$

$$\dot{v}(\mathbf{x}, 0) = 0 \qquad \text{on } \Omega, \qquad (50d)$$

$$\mathbf{s}(\mathbf{x}, 0) = 0 \qquad \text{on } \Omega, \qquad (50e)$$

$$\dot{\mathbf{s}}(\mathbf{x}, 0) = 0 \qquad \text{on } \Omega. \qquad (50f)$$

The three equations Eqs. 49a–49b are multiplied by appropriate test functions $w(\mathbf{x})$, $p(\mathbf{x})$, and $q(\mathbf{x})$, respectively, and then integrated over the entire domain Ω (regular and PML domain) to arrive at the corresponding weak forms. Again, we remark that we opted for the variational form resulting from the integration by parts of the last term in Eq. 49a; there results:

$$\int_\Omega w \left(f_m \ddot{v} + c_s \, g_c \dot{v} + c_s^2 \, g_k v \right) d\Omega$$

$$+ \int_\Omega \nabla w \cdot \left(\tilde{\mathbf{F}}^e \dot{\mathbf{s}} + \tilde{\mathbf{F}}^p \mathbf{s} \right) d\Omega = \int_\Gamma w \left(\tilde{\mathbf{F}}^e \dot{\mathbf{s}} + \tilde{\mathbf{F}}^p \mathbf{s} \right) \cdot \mathbf{n} \, d\Gamma, \qquad (51a)$$

$$\int_\Omega p \left\{ (1 + f_1^e) \frac{\partial^2 s_1}{\partial t^2} - c_s^2 \frac{\partial^2 v}{\partial x_1 \partial t} + c_s g_1^p \frac{\partial s_1}{\partial t} \right\} d\Omega = 0, \qquad (51b)$$

$$\int_\Omega q \left\{ (1 + f_2^e) \frac{\partial^2 s_2}{\partial t^2} - c_s^2 \frac{\partial^2 v}{\partial x_2 \partial t} + c_s g_2^p \frac{\partial s_2}{\partial t} \right\} d\Omega = 0, \qquad (51c)$$

where Γ denotes the boundary of Ω, and $v \in H^1$ and $\mathbf{s} \in L^2$. We remark that the term $(\tilde{\mathbf{F}}^e \dot{\mathbf{s}} + \tilde{\mathbf{F}}^p \mathbf{s}) \cdot \mathbf{n}$ vanishes on the free surface part of the PML. The trial functions

$v(\mathbf{x}, t)$, $s_1(\mathbf{x}, t)$, $s_2(\mathbf{x}, t)$ and the test functions $w(\mathbf{x})$, $p(\mathbf{x})$, $q(\mathbf{x})$ are spatially discretized as:

$$v(\mathbf{x}, t) \simeq \boldsymbol{\phi}(\mathbf{x})^{\mathrm{T}} \mathbf{v}(t), \tag{52a}$$

$$s_1(\mathbf{x}, t) \simeq \boldsymbol{\psi}(\mathbf{x})^{\mathrm{T}} \mathbf{s}_1(t), \tag{52b}$$

$$s_2(\mathbf{x}, t) \simeq \boldsymbol{\psi}(\mathbf{x})^{\mathrm{T}} \mathbf{s}_2(t), \tag{52c}$$

$$w(\mathbf{x}) \simeq \mathbf{w}^{\mathrm{T}} \boldsymbol{\phi}(\mathbf{x}), \tag{53a}$$

$$p(\mathbf{x}) \simeq \mathbf{p}^{\mathrm{T}} \boldsymbol{\psi}(\mathbf{x}), \tag{53b}$$

$$q(\mathbf{x}) \simeq \mathbf{q}^{\mathrm{T}} \boldsymbol{\psi}(\mathbf{x}). \tag{53c}$$

By contrast to the one-dimensional case, here, stable solutions are obtained when both $\boldsymbol{\phi}$ and $\boldsymbol{\psi}$ are bilinear (this is the lowest-order pair). Linear-constant and quadratic-linear pairs of approximants have resulted in instabilities.[5] Introduction of Eqs. 52c and 53 into Eq. 51 results in the following semi-discrete form:

$$
\begin{bmatrix}
\int_{\Omega} f_m \boldsymbol{\phi}\boldsymbol{\phi}^{\mathrm{T}} d\Omega & \mathbf{0} & \mathbf{0} \\
\mathbf{0} & \int_{\Omega} \left(1 + f_1^e\right) \boldsymbol{\psi}\boldsymbol{\psi}^{\mathrm{T}} d\Omega & \mathbf{0} \\
\mathbf{0} & \mathbf{0} & \int_{\Omega} \left(1 + f_2^e\right) \boldsymbol{\psi}\boldsymbol{\psi}^{\mathrm{T}} d\Omega
\end{bmatrix}
\begin{bmatrix}
\ddot{\mathbf{v}} \\
\ddot{\mathbf{s}}_1 \\
\ddot{\mathbf{s}}_2
\end{bmatrix}
$$

$$
+
\begin{bmatrix}
\int_{\Omega} c_s g_c \boldsymbol{\phi}\boldsymbol{\phi}^{\mathrm{T}} d\Omega & \int_{\Omega} \left(1 + f_2^e\right) \frac{\partial \boldsymbol{\phi}}{\partial x_1}\boldsymbol{\psi}^{\mathrm{T}} d\Omega & \int_{\Omega} \left(1 + f_1^e\right) \frac{\partial \boldsymbol{\phi}}{\partial x_2}\boldsymbol{\psi}^{\mathrm{T}} d\Omega \\
\int_{\Omega} -c_s^2 \boldsymbol{\psi} \frac{\partial \boldsymbol{\phi}^{\mathrm{T}}}{\partial x_1} d\Omega & \int_{\Omega} c_s g_1^p \boldsymbol{\psi}\boldsymbol{\psi}^{\mathrm{T}} d\Omega & \mathbf{0} \\
\int_{\Omega} -c_s^2 \boldsymbol{\psi} \frac{\partial \boldsymbol{\phi}^{\mathrm{T}}}{\partial x_2} d\Omega & \mathbf{0} & \int_{\Omega} c_s g_2^p \boldsymbol{\psi}\boldsymbol{\psi}^{\mathrm{T}} d\Omega
\end{bmatrix}
\begin{bmatrix}
\dot{\mathbf{v}} \\
\dot{\mathbf{s}}_1 \\
\dot{\mathbf{s}}_2
\end{bmatrix}
$$

$$
+
\begin{bmatrix}
\int_{\Omega} c_s^2 g_k \boldsymbol{\phi}\boldsymbol{\phi}^{\mathrm{T}} d\Omega & \int_{\Omega} c_s g_2^p \frac{\partial \boldsymbol{\phi}}{\partial x_1}\boldsymbol{\psi}^{\mathrm{T}} d\Omega & \int_{\Omega} c_s g_1^p \frac{\partial \boldsymbol{\phi}}{\partial x_2}\boldsymbol{\psi}^{\mathrm{T}} d\Omega \\
\mathbf{0} & \mathbf{0} & \mathbf{0} \\
\mathbf{0} & \mathbf{0} & \mathbf{0}
\end{bmatrix}
\begin{bmatrix}
\mathbf{v} \\
\mathbf{s}_1 \\
\mathbf{s}_2
\end{bmatrix}
=
\begin{bmatrix}
\int_{\Gamma_{\mathrm{free}}} \boldsymbol{\phi} \, p \, d\Gamma_{\mathrm{free}} \\
\mathbf{0} \\
\mathbf{0}
\end{bmatrix}. \tag{54}
$$

We use a standard Newmark-β scheme for integrating in time the semi-discrete forms Eqs. 48 and 54. We remark that the damping-like and stiffness-like matrices in Eqs. 48 and 54 are non-symmetric, and that the choice of a mixed formulation has naturally resulted in additional unknowns over standard displacement-based unsplit-field PML formulations. However, our mixed unsplit-field PML formulation has advantages over the split-field PML that entail yet more unknowns (the split fields), or other unsplit-field PML schemes that require convoluted temporal integration schemes [32], as already mentioned.

5 Numerical results

To illustrate the validity of the proposed mixed unsplit-field PML approach, we simulate the wave propagation in one- and two-dimensional semi-infinite domains truncated through the introduction of a PML.

5.1 One-dimensional examples

We consider first a one-dimensional PML-truncated semi-infinite domain subjected to a tip stress load $f(t)$ as shown in Fig. 3.

The regular domain and the PML are such that $L = 100$ m and $L_{\mathrm{PML}} = 10$ m, respectively. The density ρ is 2,000 kg/m^3, and the modulus of elasticity E is 90 MPa, which results in a wave velocity of $c = \sqrt{E/\rho} \simeq 212.132$ m/s. A step stress pulse of 10 kPa is applied at the left end for 1 s. Figure 4 shows the time history and the frequency content of the applied stress $f(t)$.
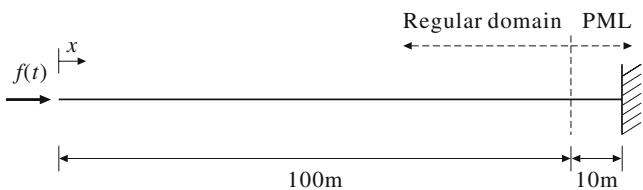

Fig. 3 A one-dimensional PML-truncated semi-infinite domain under a tip stress load $f(t)$

[5]Dispersion when using low-order approximations is exacerbated: it is an open issue, as is the case in any wave propagation simulation, and is not addressed herein.

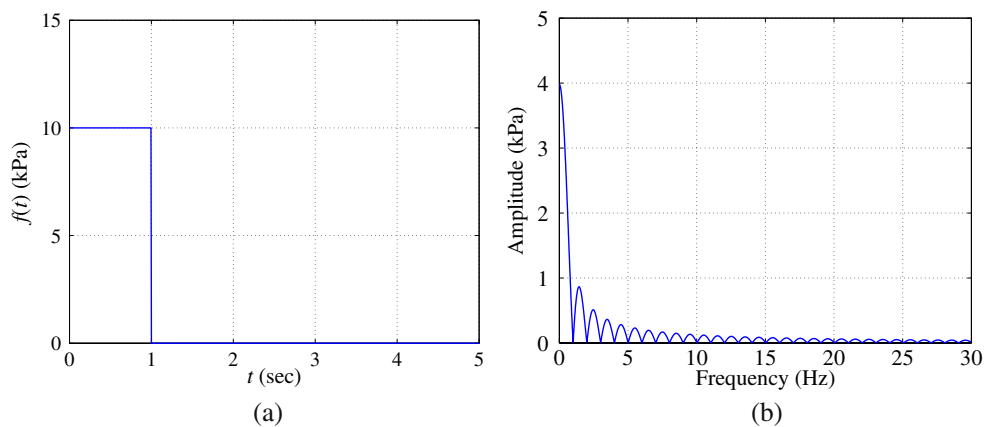**Fig. 4** **a** Time history; **b** frequency spectrum of the step stress load $f(t)$

(a)

(b)

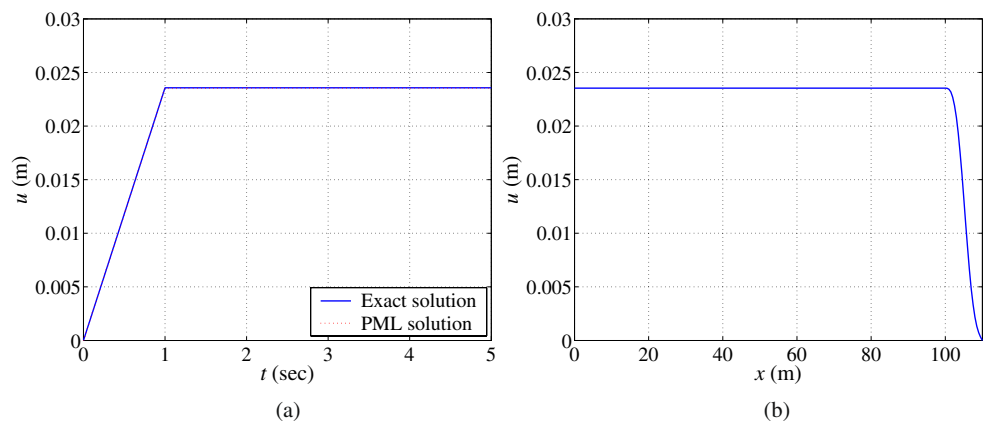**Fig. 5** **a** $u(0, t)$; exact and PML solutions; **b** snapshot of the displacement at $t = 5$ s

(a)

(b)

Fig. 6 **a** $u(0, t)$ for various reflection coefficients R; **b** $u(0, t)$ for 60 s (=12,000Δt)
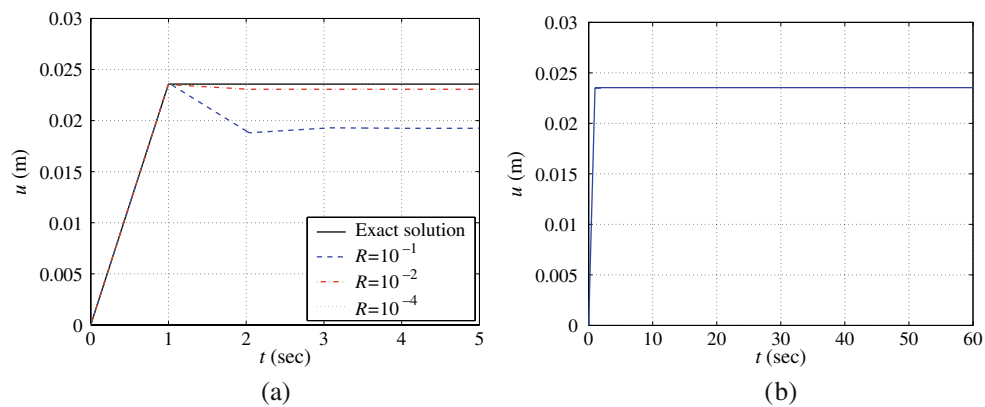

(a)

(b)

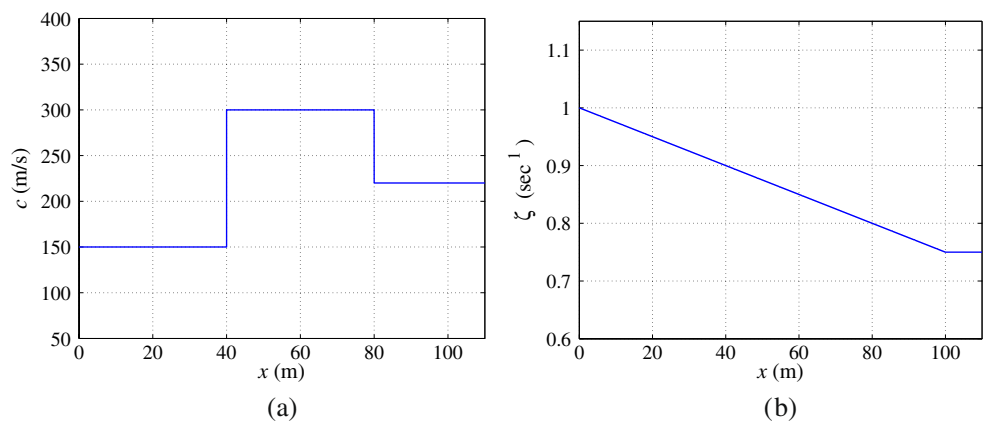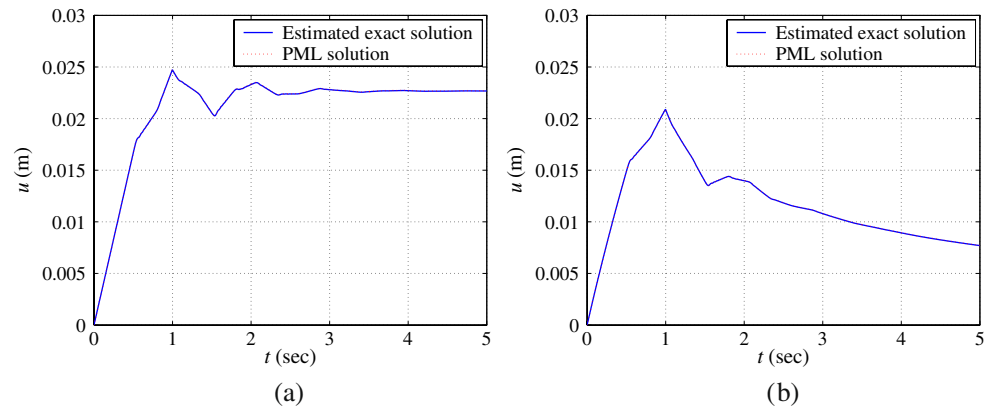**Fig. 7** **a** Heterogeneous wave velocity profile $c(x)$; **b** viscous damping profile $\zeta(x) = 1 - 0.0025x$

(a)

(b)

Fig. 8 $u(0, t)$ for an heterogeneous wave velocity profile: **a** $\zeta = 0$; **b** $\zeta = 1 - 0.0025x$

(a)

(b)

A reflection coefficient of $R = 10^{-4}$ (see Eq. 11) is imposed on the PML. The computed displacement solution at $x = 0$ is indistinguishable from the exact solution,[6] as it can be seen in Fig. 5a. Figure 5b depicts a snapshot of the displacement at $t = 5$ s, where we observe that propagating waves are attenuated rapidly within the PML without any reflection at the interface between the regular domain and the PML.

In Fig. 6a, we study the performance of the PML for several reflection coefficients R. As R gets smaller, the solution gets closer to the exact solution. We recall that R is an input parameter in the PML implementation, so that the performance of the PML can be controlled by setting the reflection coefficient appropriately. Solution stability is studied numerically using a 60-s-long simulation, which amounts to 12,000 time steps ($\Delta t = 0.005$ s). Figure 6b shows that the mixed unsplit-field PML has stable performance.

We repeat the same experiment for a heterogeneous domain with wave velocity and damping profiles as shown in Fig. 7. Figure 8a and b depict the displacement response at $x = 0$ in the layered medium without and with damping, respectively. The PML solutions are almost the same as the estimated exact solutions, which are computed by using an extended computational domain that ensures that any reflected waves will not arrive at the left end for the first 5 s, during which we record the response.

5.2 Error studies

We are concerned with errors arising from the numerical implementation of the mixed PML scheme. We discuss two possible sources of error: firstly, discretization error in light of our adoption of a mixed method, and

secondly, reflection error from the fixed boundary at the edge of the PML domain due to the user-defined reflection coefficient $|R|$. We are especially interested in

- Error behavior with respect to element length variations
- Effect of PML parameters (L_{PML}, $|R|$) on errors

5.2.1 Homogeneous domain case

We use the prototype problem illustrated in Fig. 1 to study errors. We set the domain length at $L = 2$, the wave velocity at $c = 5$, and the density at $\rho = 1$ (we henceforth drop units for convenience). We use a uniform mesh comprising elements of length h. A sine stress load $p(t) = \sin(t)$ of unit amplitude is applied at
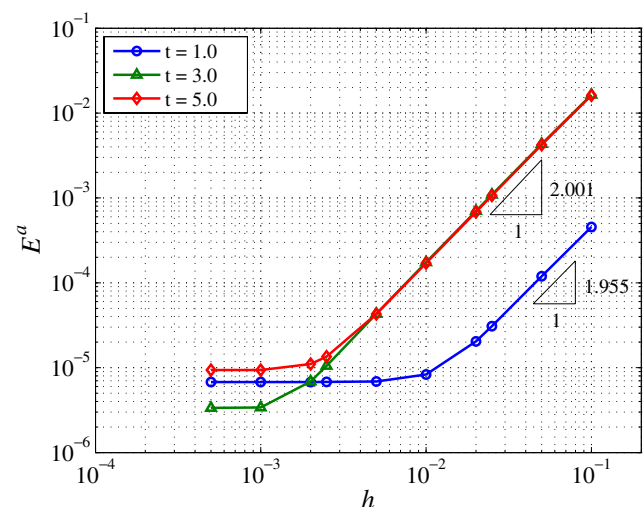

Fig. 9 L^2-norm error (E^a) versus h for $t = 1, 3, 5$ ($L_{PML} = 0.4$, $R = 10^{-6}$); homogeneous domain case

---

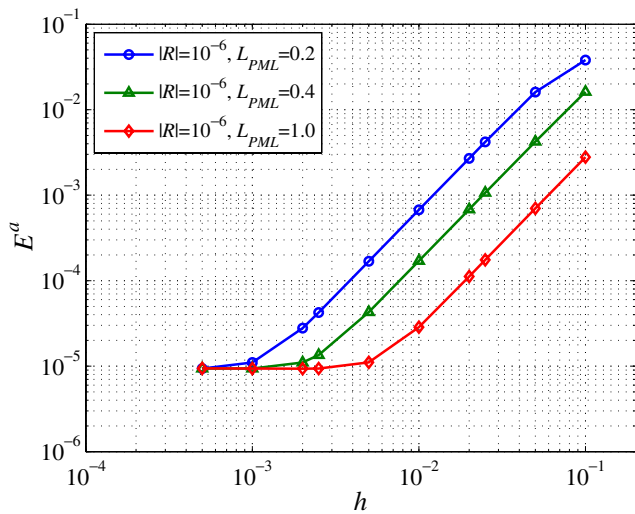[6]Since the domain is homogeneous, the exact response can be easily obtained by placing a dashpot at $x = L$.

Fig. 10 L^2-norm error (E^a) versus h for $L_{PML} = 0.2, 0.4, 1.0$ ($R = 10^{-6}$, $t=5$); homogeneous domain case
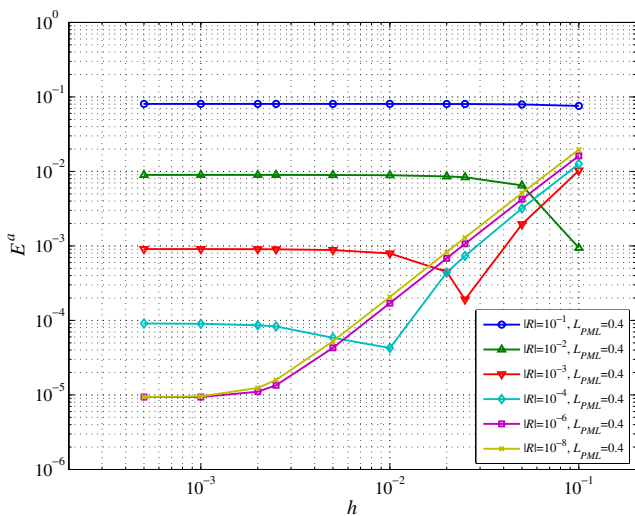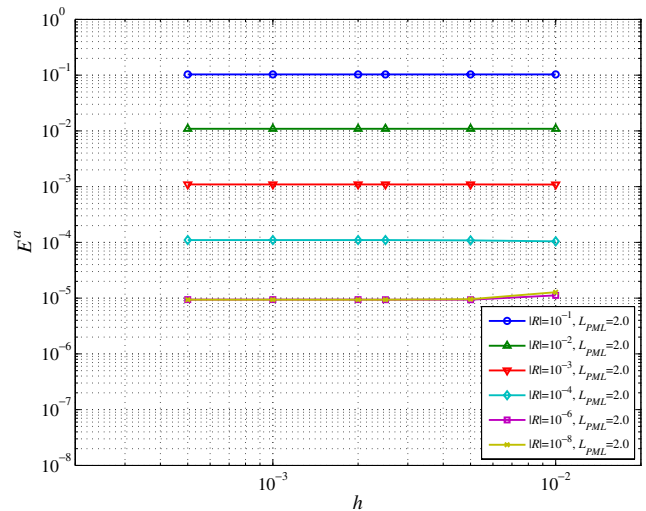

Fig. 12 L^2-norm error (E^a) versus h for $|R| = 10^{-1}, 10^{-2}, 10^{-3}, 10^{-4}, 10^{-6}, 10^{-8}$ ($L_{PML} = 2.0$); homogeneous domain case

the left end ($x = 0$) of the domain. With these definitions, the dominant wavelength corresponding to the excitation is, by design, fairly large compared to the domain length ($\sim 31.4:2$). We are interested in the behavior of the error $e = u_{ex} - u_h$ in the time-dependent L^2-norm:

$$E^a(t) = \left[\int_0^L \{u_{ex}(x, t) - u_h(x, t)\}^2 \, dx \right]^{\frac{1}{2}}, \qquad (55)$$

where u_{ex} is the exact solution and u_h is the approximate solution. u_{ex} is obtained by directly solving the

wave equation $u_{tt} = c^2 u_{xx}$, given the stress boundary condition $\rho c^2 \partial u / \partial x(0, t) = p(t)$. Accordingly:

$$u_{ex}(x, t) = \frac{1}{5\rho} \int_0^\infty \sin(\tau) H \left(t - \tau - \frac{x}{5} \right) d\tau, \qquad (56)$$

in which $H(\cdot)$ is the Heaviside step function.

Figure 9 depicts the L^2-norm errors against h, sampled at different times $t = 1, 3,$ and 5, respectively. The PML parameters for this experiment are $L_{PML} = 0.4$ (20% of the regular domain size) and $|R| = 10^{-6}$. As it can be seen from the figure, the theoretically expected convergence rate of $O(h^2)$ is attained. Notice also that, as h becomes smaller, the total error is dominated by the reflection error, which depends on the reflection parameter R, with the discretization error having a negligible effect ("flat" region).

To study the effect of the PML size L_{PML} on the error, we set again the regular domain size to $L = 2$

Fig. 11 L^2-norm error (E^a) versus h for $|R| = 10^{-1}, 10^{-2}, 10^{-3}, 10^{-4}, 10^{-6}, 10^{-8}$ ($L_{PML} = 0.4$); homogeneous domain case
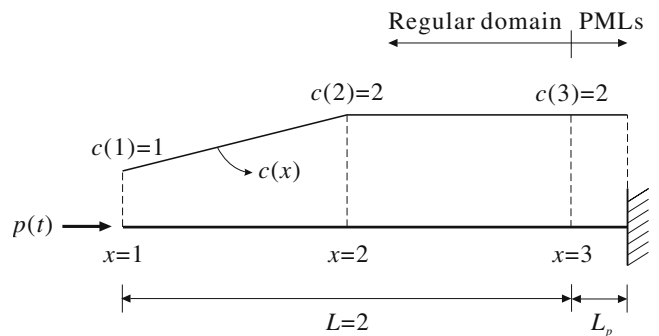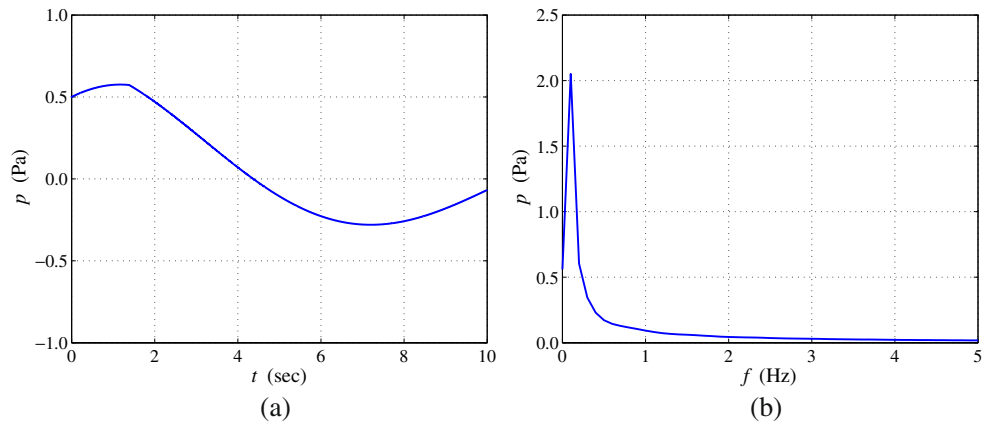

Fig. 13 A one-dimensional heterogeneous semi-infinite domain with PMLs as the wave absorbing boundary layers

Fig. 14 a Time history of the stress load $p(t)$ applied at the left end of a heterogeneous domain; **b** frequency spectrum of $p(t)$

and test for $L_{\text{PML}} = 0.2,\ 0.4,\ 1.0$. Figure 10 shows that the L^2-norm error (E^a) decreases as the PML length (L_{PML}) increases, for fixed $|R|$ values (all curves are plotted for $t = 5$, and are representative of other times as well; $|R| = 10^{-6}$). Thus, a longer PML results in stronger attenuation and presents the fixed boundary at L_t with smaller amplitudes, such that the overall error becomes smaller.

Next, we let the reflection parameter $|R|$ vary while keeping the PML length fixed at $L_{\text{PML}} = 0.4$. Figure 11 depicts the L^2-norm for a fixed $t = 5$, and for six different $|R|$ values. Here, we reaffirm the earlier observation we made based on the results shown in Fig. 9, which is that, for smaller h, the total error is dominated by the reflection error, as evidenced by the flat portion of all curves. Moreover, for $|R|$ smaller than 10^{-5} and for all cases for which the discretization error is not defeated by the reflection error, the convergence rate

is optimal. Notice, that, for higher values of $|R|$, and for specific mesh sizes (e.g., $h = 0.1, 0.01$), there seems to exist an optimal reflection coefficient; at present, we do not have an adequate explanation for this behavior.

Next, we fix the PML size at 2.0, i.e., me make the PML buffer zone as large as the regular domain and experiment with different values of R. Figure 12 suggests that the error is now solely controlled by the effects of the reflection coefficient, for any h. In practice, it is, of course, prohibitive to use such a large PML due to the radical increase in computational cost, especially for two- or three-dimensional problems. Keeping in mind the observations made herein, it is recommended that one uses R values less than 10^{-3}, while keeping as fine a mesh in the PML zone as in the regular domain. We remark that our observations are based on a relatively low-frequency excitation: this is by design, since it is in
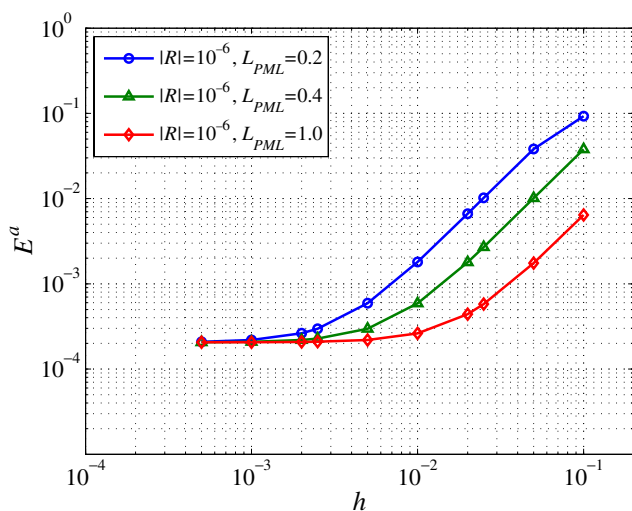

Fig. 15 L^2-norm error (E^a) plotted against h for $L_{\text{PML}} = 0.2, 0.4, 1.0$ ($R = 10^{-6}$, $t = 5$ s); heterogeneous domain case
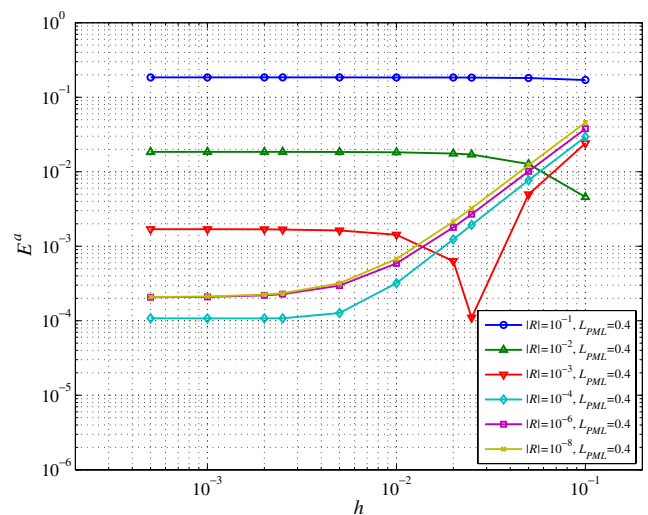

Fig. 16 L^2-norm error (E^a) plotted against h for $|R| = 10^{-1}$, $10^{-2}, 10^{-3}, 10^{-4}, 10^{-6}, 10^{-8}$ (L_{PML} is kept to be 0.4); heterogeneous domain case
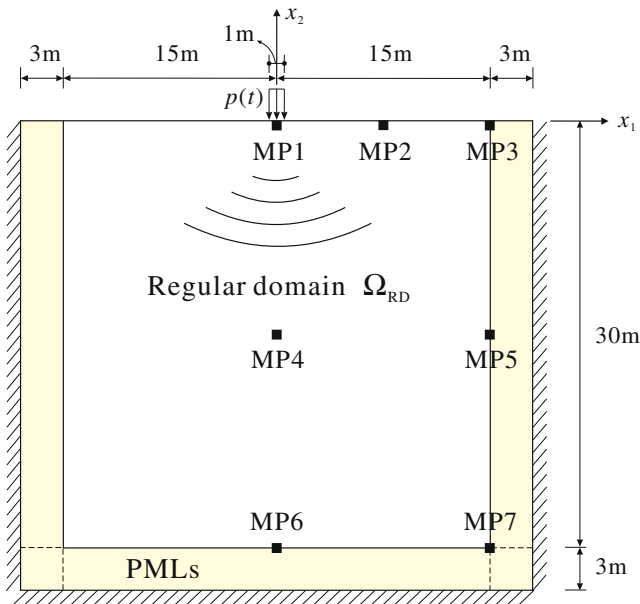
Fig. 17 A PML-truncated two-dimensional half-plane subjected to a shear stress load (σ_{32}) on its surface; the response is sampled at MPi, with $i = 1, \ldots, 7$

the low-frequency regime that most transparent, local or non-local, or absorbing conditions fail or have difficulty with. It also appears that a fraction ($< 10\%$) of the regular domain's size is sufficient for attenuating waves.

We remark that, within the PML, the required mesh density greatly depends on the sharpness of the imposed attenuation profile. That is, even if the element size is sufficiently small to resolve the propagating waves (i.e., have a sufficient number of points per wavelength), a sharply varying attenuation profile may impose more onerous requirements on the element size in order for the mesh to adequately capture the amplitude decay. The sharpness of the profile depends on the polynomial order of the attenuation function, on the PML length, and on the reflection coefficient R Eq. 7. For example, smaller values of R create profiles that result in rapid attenuation close to the interface, having a smoother transition closer to the fixed boundary, whereas, by contrast, higher R values result in smoother transition close to the PML interface, and decay sharply as the fixed boundary is approached. Therefore, using elements of variable size within the PML that adequately resolve the decaying profiles, irrespective of where the profile sharpness may manifest, has merit (a one-sided such refinement was suggested in

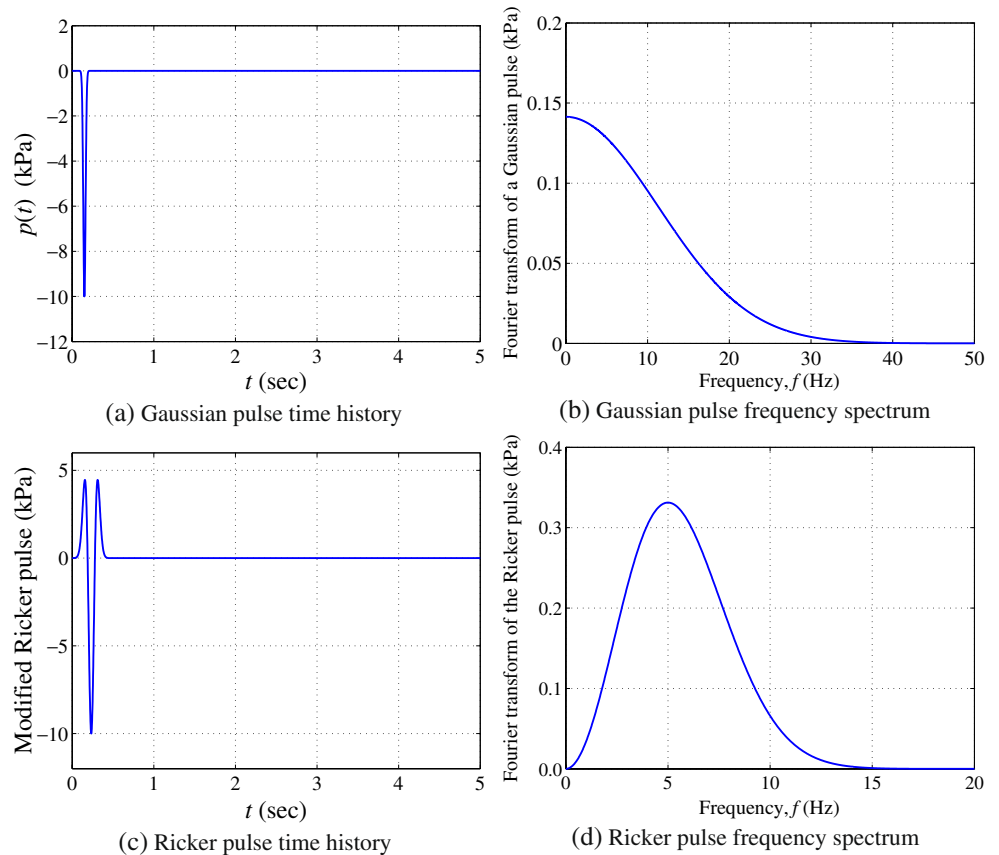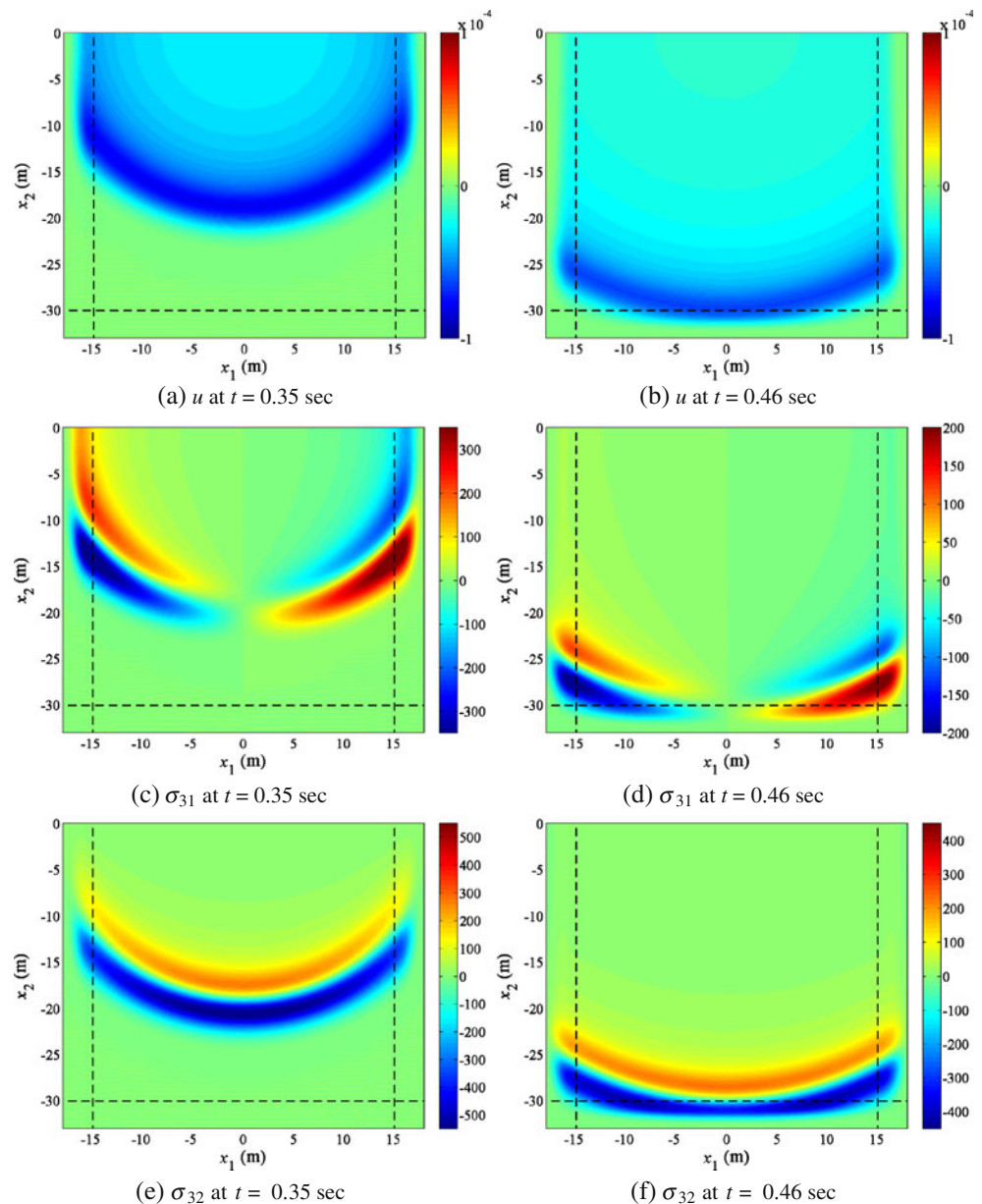**Fig. 18** Excitation time signals and their Fourier spectrum

(a) Gaussian pulse time history

(b) Gaussian pulse frequency spectrum

(c) Ricker pulse time history

(d) Ricker pulse frequency spectrum

Fig. 19 Snapshots of u, σ_{31}, and σ_{32} using a Gaussian pulse excitation with maximum frequency $f_{max} = 40$ Hz

(a) u at $t = 0.35$ sec

(b) u at $t = 0.46$ sec

(c) σ_{31} at $t = 0.35$ sec

(d) σ_{31} at $t = 0.46$ sec

(e) σ_{32} at $t = 0.35$ sec

(f) σ_{32} at $t = 0.46$ sec

[64]), since it stands to impact the computational cost. In this work, we have only experimented with uniform meshes, as the impact of the PML mesh density on the computational cost is minimal.

5.2.2 Heterogeneous domain case

Next, we turn to heterogeneous domains: Fig. 13 depicts the regular domain exhibiting a two-part modulus profile, linear at the beginning and constant beyond the half point. A stress load $p(t)$ is applied at the left end of the domain.[7] The time signal $p(t)$ and its frequency
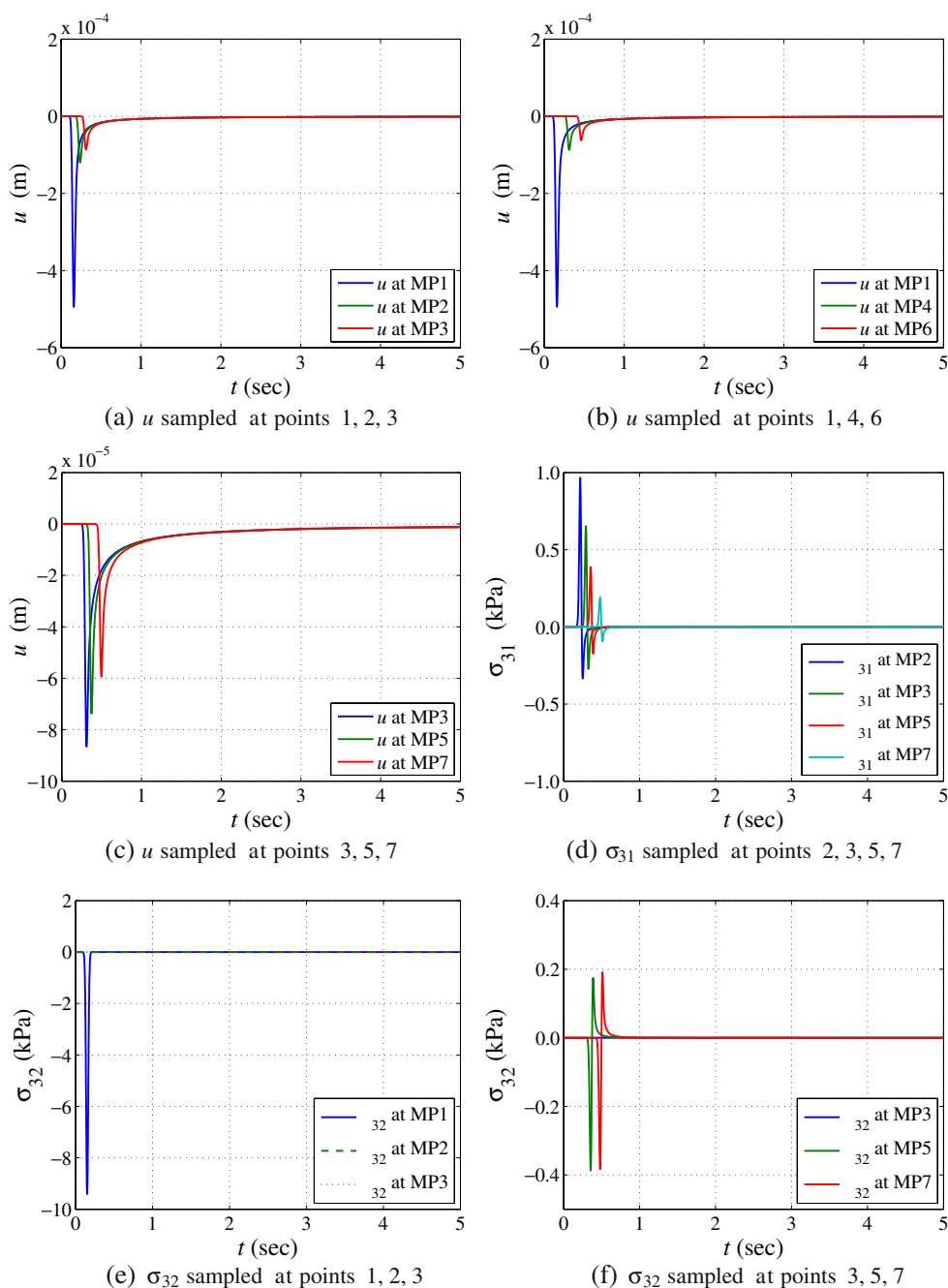
spectrum are shown in Fig. 14. Due to the simplicity of the modulus profile, an exact solution is recoverable,[8] and is used to drive the error analysis.

Figure 15 depicts the L^2 error against h for various PML lengths, whereas Fig. 16 shows the effect of the reflection coefficient $|R|$ on the error when L_{PML} is kept fixed. The observations made earlier in the homogeneous case are re-affirmed in the heterogeneous case: that is, when h is small, the simulation error is controlled by R, and the performance is optimal ($O(h^2)$) when R is small enough.

---

[7]See Appendix A for the specific form of $p(t)$.

[8]Also in Appendix A.

Fig. 20 Various domain point time histories for the Gaussian pulse excitation

(a) u sampled at points 1, 2, 3

(b) u sampled at points 1, 4, 6

(c) u sampled at points 3, 5, 7

(d) σ_{31} sampled at points 2, 3, 5, 7

(e) σ_{32} sampled at points 1, 2, 3

(f) σ_{32} sampled at points 3, 5, 7

5.3 Two-dimensional examples

To demonstrate the applicability and performance of the mixed PML scheme in the two-dimensional SH wave propagation case, we treat both homogeneous and heterogeneous problems.

5.3.1 Homogeneous half-plane

Consider first a 30×30-m truncated half-plane, where PMLs (3 m wide) have been introduced on the sides

and bottom of the truncated domain, as shown in Fig. 17. The domain is homogeneous with density $\rho = 2,000 \text{ kg/m}^3$ and shear wave velocity $c_s = 100$ m/s. The combined regular and PML domains are discretized using bilinear or biquadratic elements with an element size of 0.25m.[9] There result 12 elements within each PML region. A reflection coefficient $|R| = 10^{-4}$ is used, and a stress load $\sigma_{32} = p(t)$ is applied over a small

---

[9]We used bilinear elements for the Gaussian pulse cases, and biquadratic for the Ricker pulse cases.

Fig. 21 Snapshots of u, σ_{31}, and σ_{32} using a Ricker pulse excitation with central frequency $f_r = 5$ Hz

(a) u at $t = 0.47$ sec

(b) u at $t = 0.55$ sec

(c) σ_{31} at $t = 0.47$ sec

(d) σ_{31} at $t = 0.55$ sec

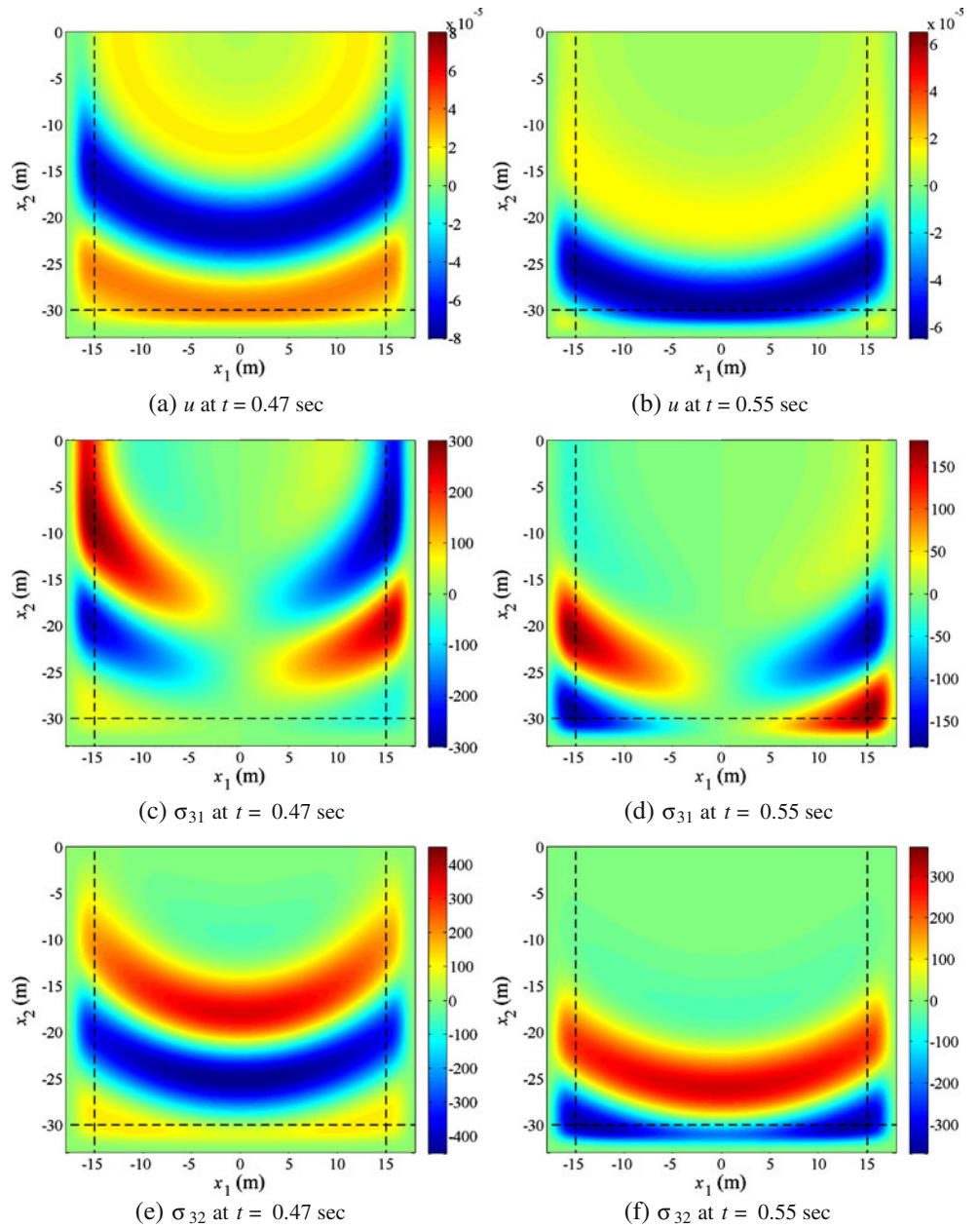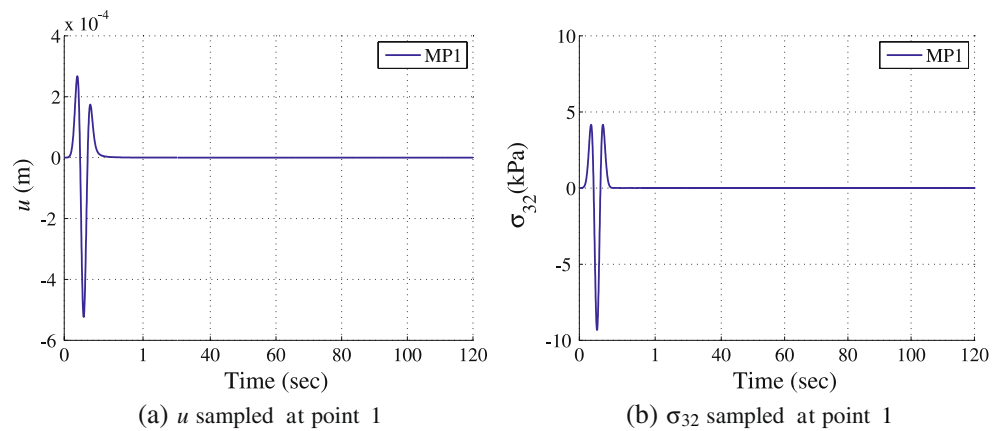(e) σ_{32} at $t = 0.47$ sec

(f) σ_{32} at $t = 0.55$ sec

Fig. 22 Numerically stable, extended, displacement, and stress time histories due to a Ricker pulse excitation ($f_r = 5$ Hz)

(a) u sampled at point 1

(b) σ_{32} sampled at point 1

(a) Total energy $E(t)$ within Ω_{RD}

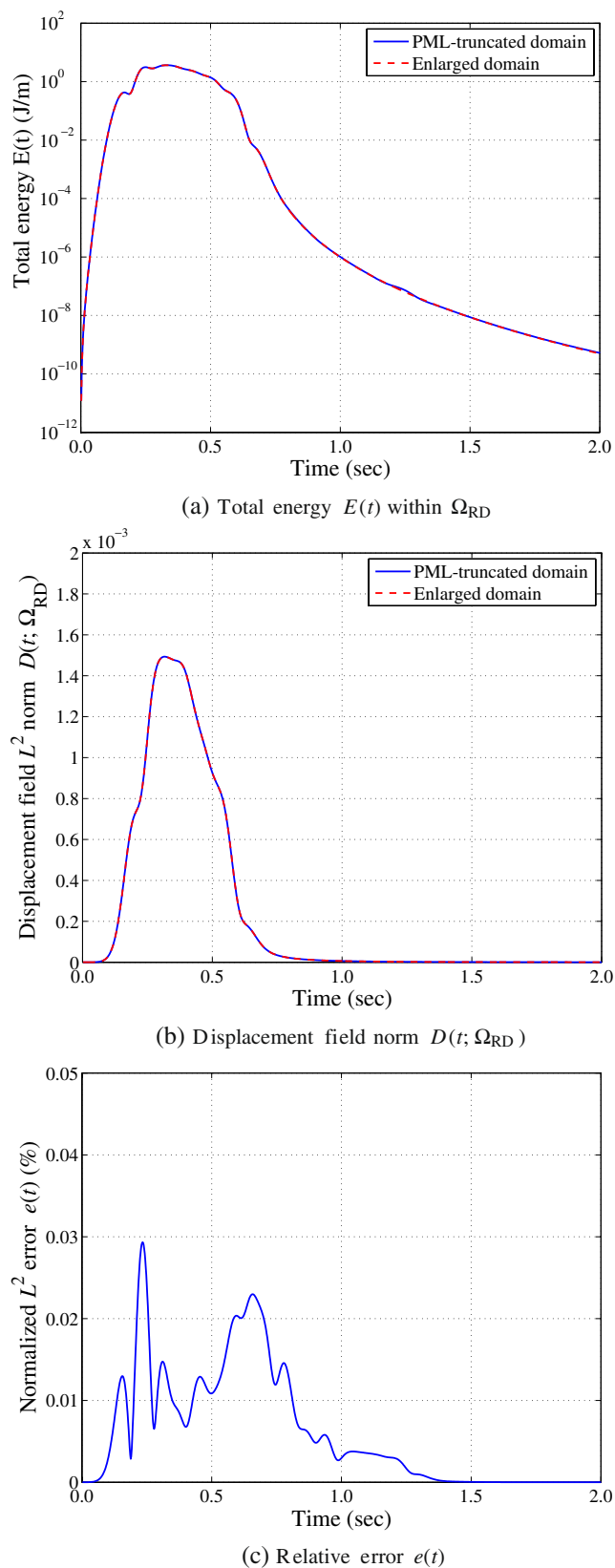(b) Displacement field norm $D(t; \Omega_{RD})$

(c) Relative error $e(t)$

Fig. 23 Energy and error metrics for the homogeneous domain excited by a surface Ricker pulse ($f_r = 5$ Hz)

region (-0.5 m $\leq x_1 \leq 0.5$ m) on the top surface of the domain. We use seven locations (MPi) to sample the time histories of the anti-plane displacement (u), and of the two shear stresses (σ_{31}, σ_{32}), respectively.

To illuminate the domain, we use both a Gaussian pulse (Fig. 18a, b) with a broad frequency spectrum and a Ricker pulse (Fig. 18c, d) with narrower frequency support and a central frequency $f_r = 5$ Hz.[10] In all numerical simulations, we used a time step of 0.002 s. Figure 19 shows snapshots of the displacement u, $\sigma_{31} = \dot{s}_1$, and $\sigma_{32} = \dot{s}_2$, respectively, at two distinct times. As can be seen in the figures, there are no observable reflections propagating back to the regular domain for either the displacement or any of the two stress waves.

Figure 20 depicts displacement and stress time histories for 5 s at various monitoring points throughout the domain. All responses are seen to (a) obey causality and (b) be clear of reflections (there are no discernible spurious oscillations), including points on the regular-PML domain interface (3, 5, 6, and 7). Notice that no instabilities are observable after 2,500 time steps.

Snapshots of the displacement and two shear stresses when using the Ricker pulse are shown in Fig. 21. For this narrower band excitation, there are again no discernible reflections for either the displacement or the stress waves, even in the neighborhood of the corner layers.

Next, we provide numerical evidence of the stability of the two-dimensional mixed PML scheme: Fig. 22 depicts the displacement and stress response under the load (at MP1) due to a Ricker pulse with a central frequency of $f_r = 5$ Hz applied in a manner similar to the preceding examples. This time, the simulation is carried out for 120 s, effectively requiring 60,000 time steps. As can be seen in the figure, the response is stable (notice that the abscissa has been compressed for times greater than 1 s to show the short-term response and the long-term stability).

Lastly, we provide error and energy metrics to quantify the performance. To assess errors for problems for which exact solutions do not exist, we embed the regular domain Ω_{RD} within an enlarged domain Ω_{LD}, whose outer boundaries are fixed. We use a displacement-based formulation to compute the response within the enlarged domain Ω_{LD} (there are no PMLs for the enlarged domain), while ascertaining that we record the response up to times prior to the arrival of the reflections from the fixed outer boundaries of the enlarged domain. We compare the response only within the regular domain Ω_{RD}. To ease the comparisons, we

---

[10]See Appendix B for the Gaussian and Ricker pulse expressions.

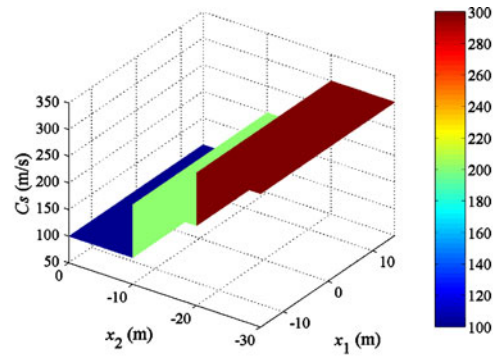**Fig. 24** A smooth profile domain and associated response
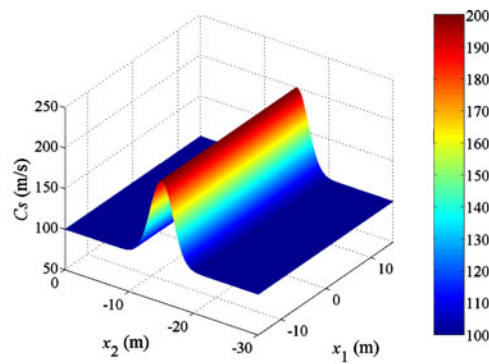
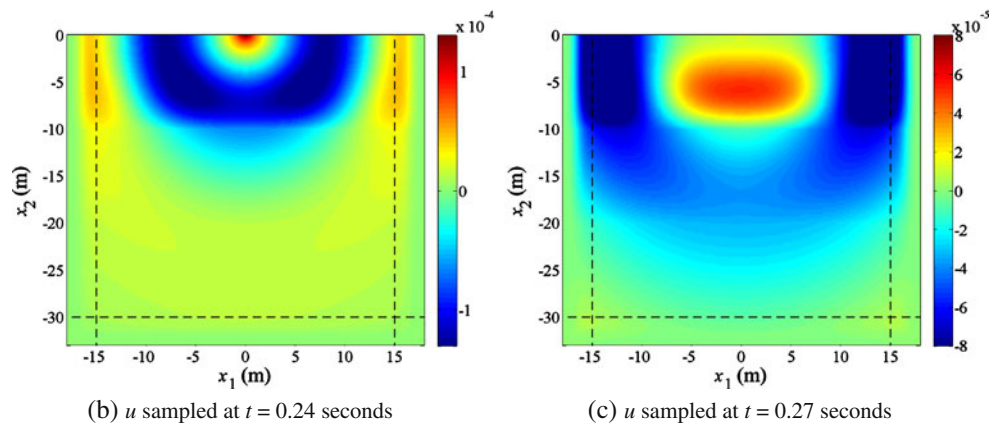(a) A PML-truncated heterogeneous domain with smoothly-varying shear wave velocity profile
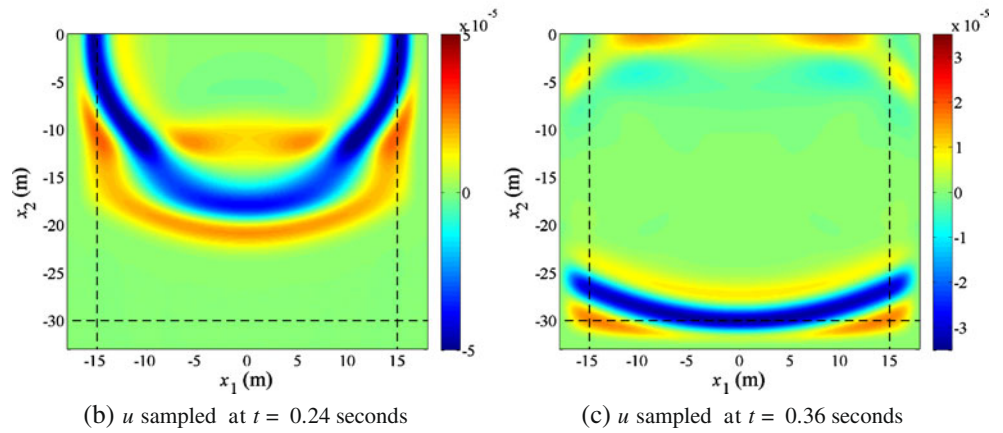
(b) *u* sampled at *t* = 0.24 seconds

(c) *u* sampled at *t* = 0.36 seconds

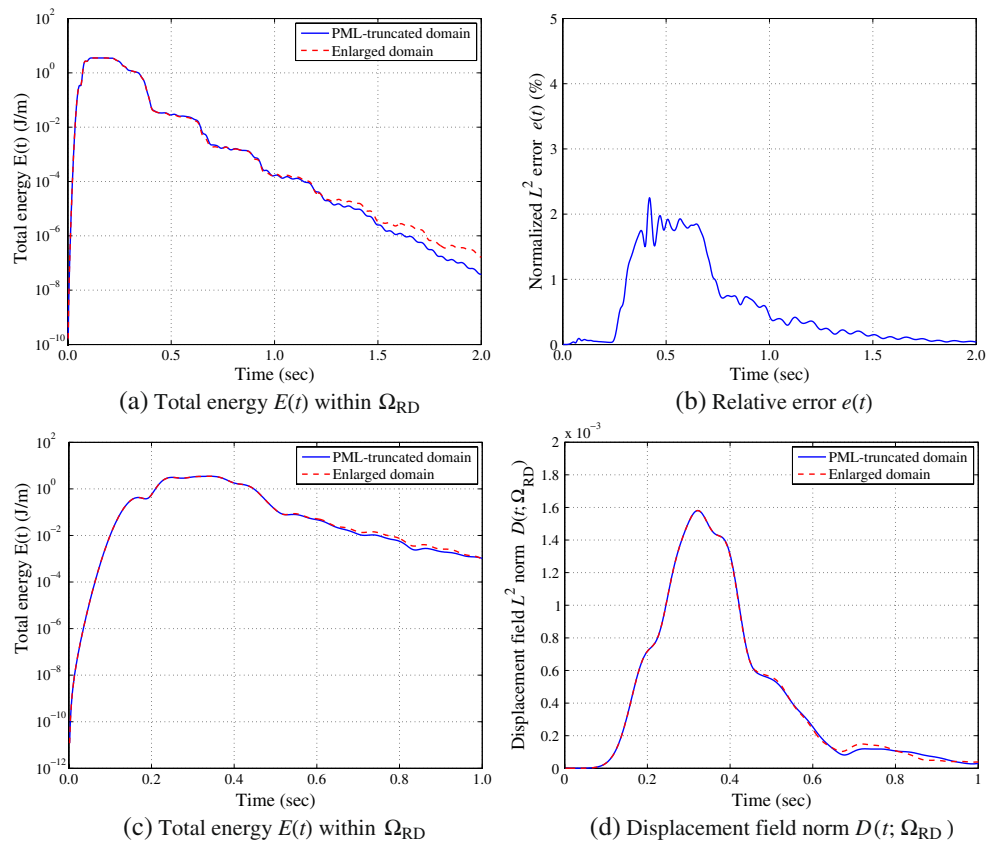**Fig. 25** A layered domain and associated response

(a) PML-truncated layered domain

(b) *u* sampled at *t* = 0.24 seconds

(c) *u* sampled at *t* = 0.27 seconds

Fig. 26 Energy and error metrics for heterogeneous domains; **a** and **b** pertain to the smoothly varying heterogeneous profile and are due to a Ricker pulse with $f_r = 15$ Hz; **c** and **d** pertain to the layered profile and are due to a Ricker pulse with $f_r = 5$ Hz

(a) Total energy $E(t)$ within Ω_{RD}

(b) Relative error $e(t)$

(c) Total energy $E(t)$ within Ω_{RD}

(d) Displacement field norm $D(t; \Omega_{RD})$

introduce three metrics; we define first the L^2 norm of the displacement field over a domain Ω as:

$$D(t; \Omega) = \left[\int_\Omega u^2(\boldsymbol{x}, t) d\Omega \right]^{\frac{1}{2}}. \tag{57}$$

Next, we define the time-dependent relative error in terms of L^2 norms, normalized with respect to the peak value of the L^2 norm within the enlarged domain, as:

$$e(t) = \frac{\left\{ \int_{\Omega_{RD}} [u(\boldsymbol{x}, t) - u_{LD}(\boldsymbol{x}, t)]^2 d\Omega_{RD} \right\}^{\frac{1}{2}}}{\max_t D_{\Omega_{LD}}(t)} \times 100. \tag{58}$$

As a third metric, we use the total energy, defined as:

$$E(t) = \frac{1}{2} \int_\Omega \rho \left(\frac{\partial u}{\partial t} \right)^2 d\Omega + \frac{1}{2} \int_\Omega \frac{\boldsymbol{\sigma}^T \boldsymbol{\sigma}}{2\rho c_s^2} d\Omega. \tag{59}$$

We compute the total energy always only within the regular domain Ω_{RD}. Figure 23a shows, in a semilog plot, the comparison between the energy computed based on the mixed method and using only the PML-truncated domain, against the energy computed based on the displacement-based method for the enlarged domain, respectively. The agreement is excellent.

Figure 23b shows a comparison of the time-dependent displacement norms $D(t)$, while Fig. 23c shows the normalized time-dependent error $e(t)$ in percent, which is below 0.03% at all times.
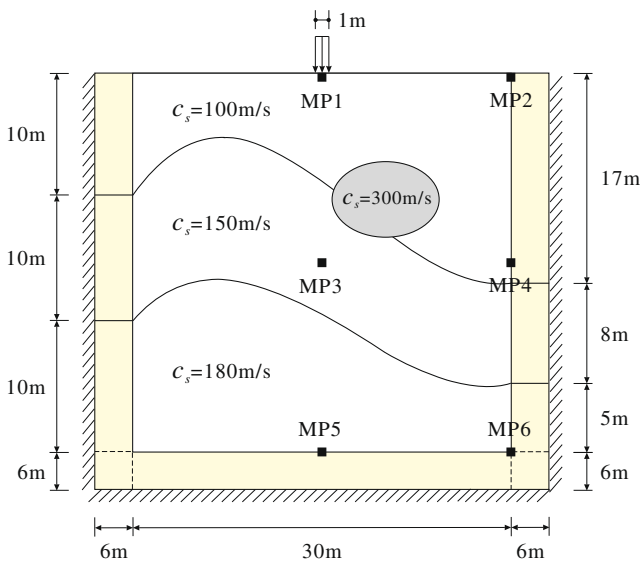
5.3.2 Heterogeneous domain case

We consider next two distinct heterogeneous profiles, one where the shear wave velocity varies smoothly, and one where the profile is sharply varying, as is typically the case with layered media. Specifically, for the former case, we consider,

$$c_s(x_1, x_2) = 100 + 100 \exp \left[-\frac{(x_2 + 15)^2}{6} \right] \left(\frac{\mathrm{m}}{\mathrm{s}} \right), \tag{60}$$
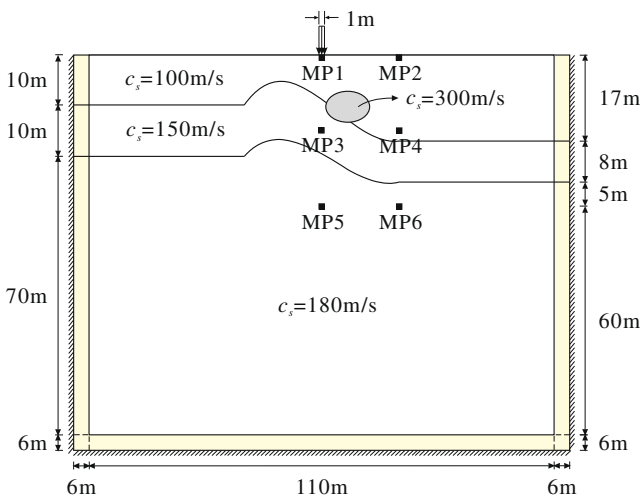
whereas, for the latter, we define:

$$c_s = 100 \text{ m/s} \quad \text{for } -10\mathrm{m} \leq x_2 \leq 0\mathrm{m},$$
$$c_s = 200 \text{ m/s} \quad \text{for } -20\mathrm{m} \leq x_2 < -10\mathrm{m},$$
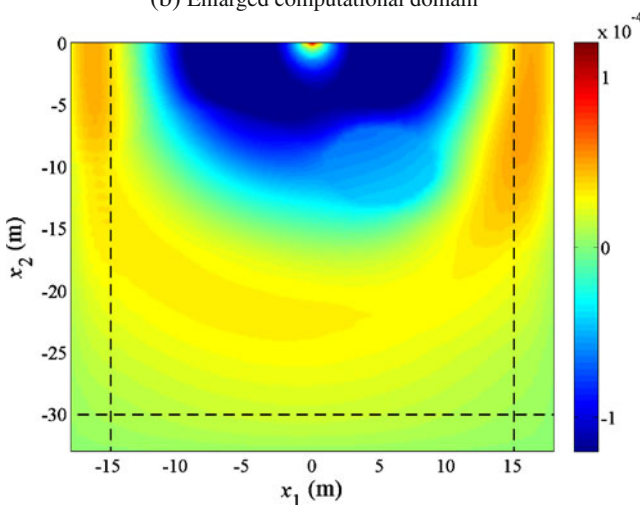$$c_s = 300 \text{ m/s} \quad \text{for} \quad x_2 < -20\mathrm{m}. \tag{61}$$

Within the PML regions, the shear wave velocity is constant along lines perpendicular to the regular domain–PML interface, and equal in value to the velocity at the

(a) PML-truncated inclined-layer heterogeneous domain

(b) Enlarged computational domain

(c) *u* sampled at *t* = 0.386 seconds

Fig. 27 An inclined-layer heterogeneous domain and associated response

interface. In other words, within, for example, the right-side PML, there is heterogeneity along the depth (x_2), but homogeneity along each x_1 abscissa, that is:

$$c_s(x_1, x_2) = c_s(x_{PML}, x_2), \quad x_1 \geq x_{PML}. \tag{62}$$

The same approach to assigning properties within the side PML regions applies to the bottom PML zone. At the two corner regions, uniform properties are assigned equal to the properties of the regular domain's corner point. Figure 24a shows the smooth velocity profile, and Fig. 24b, c depicts snapshots of the displacement response taken at two different times due to a Ricker pulse excitation with a central frequency of $f_r = 15$ Hz. In Fig. 24b, the wave front is just passing through the high-velocity region of the profile (peak of the bell curve), whereas in Fig. 24c, one could see that reflections due to the material heterogeneity have reached the top surface while the front is just reaching the bottom PML zone. Similarly, Fig. 25 depicts the profile and response of a layered system due to a Ricker pulse with a central frequency of $f_r = 5$ Hz. In both cases, reflections from the PML interface are not discernible.

To provide error metrics associated with the heterogeneous cases, we repeat the calculations over enlarged domains using a displacement-based formulation and fixed outer boundaries. We embed the computational domain of interest within the enlarged domain, as we did for the homogeneous case reported earlier. Since, in these cases, the domain is heterogeneous, we extend the heterogeneity within the enlarged domain as follows: for the smoothly varying profile case, we extend the heterogeneity only laterally, keeping the profile homogeneous below the 30-m mark at $c_s = 100 \frac{m}{s}$. For the layered case, we again extend the heterogeneity laterally, while keeping the profile homogeneous at $c_s = 200 \frac{m}{s}$, below the third layer. Figure 26 shows energy and error curves for the two cases. The differences in the energy between the enlarged and PML-truncated domains are negligible, while the normalized L^2 error is below 2.5%.

Lastly, we report results for the heterogeneous domain depicted in Fig. 27a comprising inclined layers (possibly non-physical), and an inclusion with a material contrast ratio of 3:1 when compared with the softest layer.[11] The excitation is again a Ricker pulse with a central frequency $f_r = 4$ Hz; the element length is 0.5 m and the time step is $\Delta t = 0.002$ s. The resulting smallest wavelength is approximately 8 m, somewhat large to generate strong reflections from the layers
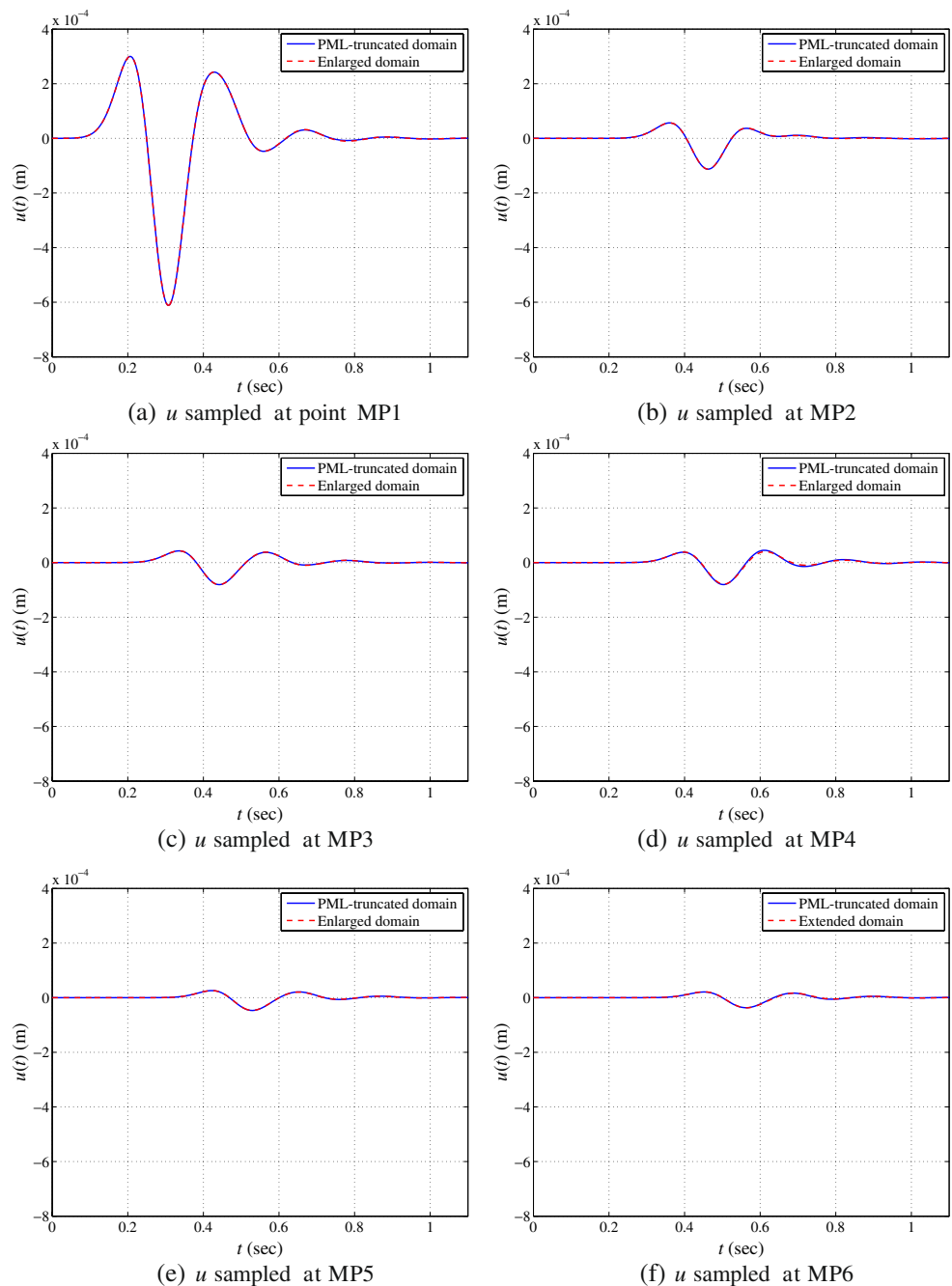
---

[11]The inclined layer profile has been generated using a cubic polynomial.

and/or the inclusion, but still sufficient for discernible manifestation of the heterogeneity. Figure 27c shows a snapshot of the displacement wave at $t = 0.386$ s, where the presence of the inclusion is clearly seen to affect the propagation patterns.

Next, we report the displacement histories at the six monitoring stations MPi depicted in Fig. 27a. Moreover, we enlarge the computational domain, as per Fig. 27b, by simply extending the layers in a horizontal manner, and collect anew the response at the same monitoring stations. In the enlarged domain case, we try to ensure that the records are not polluted by any potential reflections from the PML structures, by recording up to times for which such reflections, if they exist at all, do not have sufficient time to travel back to the monitoring stations. Figure 28 provides a comparison between the histories at the same points of the original and enlarged domains: the agreement

Fig. 28 Response time histories at monitoring stations—inclined-layer domain

(a) u sampled at point MP1

(b) u sampled at MP2

(c) u sampled at MP3

(d) u sampled at MP4

(e) u sampled at MP5

(f) u sampled at MP6

is remarkable, despite the fact that the PML has been constructed without taking into account the stratification of the exterior domain that was excluded from the computations in the first case.

6 Conclusions

In this article, we attempted to fill a gap in the array of methods available for the simulation of waves in heterogeneous domains by discussing the development of a new displacement-stress mixed finite element formulation for PML-truncated infinite or semi-infinite domains. The motivation, as discussed, stemmed from needs arising in total wavefield-based inversion, where existing split-field, or displacement-based unsplit-field PML techniques are either unsuitable or too cumbersome to implement, especially in the context of adjoint-field formulations.

The formulation is simple and was shown to retain the second-order temporal character of the original problem. Both displacement and stress waves are attenuated within the PML zone, with excellent absorption characteristics. Numerically, as the results demonstrate, we have not observed either instabilities or non-causal behavior. For stability, we proposed a linear–constant pair in one dimension, and a linear–linear pair in two dimensions: these were the lowest-order pairs that were numerically shown to be stable. Higher-order pairs are possible, and will assist in combating dispersion, which has not been addressed here; the specific orders can be found through formal analysis of the inf-sup condition.

The magnitude of the reflection coefficient imposed at the fixed outer boundaries of the PML zones is of importance in the numerical simulations: at fine discretizations, it dominates the simulation error: experientially, and supported by the discussed results, we recommend values below 10^{-3}. The size of the PML zone does not appear to critically affect the quality of the results: larger PML zones are beneficial, but a clear trade-off point between computational cost and PML size is highly problem-dependent.

Lastly, we remark that the computational cost of the mixed method is comparable to split-field methods, and costlier than unsplit-field displacement-based formulations. However, our approach has an advantage over the latter, given the implementational ease that avoids complicated temporal integration schemes.

Appendix A: One-dimensional heterogeneous domain exact solution

For the following tip load,

$$
\begin{aligned}
p(t) = {} & \frac{1}{4}\left\{\cos\left(\frac{1}{2}t\right) + \sin\left(\frac{1}{2}t\right) + J_0\left(\frac{1}{2}t\right)\right\} \\
& + \frac{1}{8}\int_0^\infty J_0\left(\frac{1}{2}\sqrt{(t-\tau)^2 - (2\ln 2)^2}\right) \\
& \times \left\{J_1\left(\frac{1}{2}\tau\right) - J_0\left(\frac{1}{2}\tau\right)\right\} \\
& \times H(t - \tau - 2\ln 2)\,d\tau,
\end{aligned}
\tag{63}
$$

the exact solution to the wave equation for the modulus profile depicted in Fig. 13 and for a unit density, can be shown to be:

$$
\begin{aligned}
u_{\mathrm{ex}}(x,t) = {} & \frac{1}{\rho}e^{-\frac{1}{2}\ln x} \\
& \times\Bigg[\frac{1}{8}\int_0^\infty\int_0^\infty J_0\left(\frac{1}{2}\tau\right) \\
& \times J_0\left(\frac{1}{2}\sqrt{(t-\theta-\tau)^2 - (2\ln 2 - \ln x)^2}\right) \\
& \times H(t-\theta-\tau - 2\ln 2 + \ln x)\,d\tau\,d\theta \\
& -\frac{1}{8}\int_0^\infty\int_0^\infty J_0\left(\frac{1}{2}\tau\right) \\
& \times J_0\left(\frac{1}{2}\sqrt{(t-\theta-\tau)^2 - (\ln x)^2}\right) \\
& \times H(t-\theta-\tau - \ln x)\,d\tau\,d\theta \\
& +\frac{1}{4}\int_0^\infty\left\{1 - J_0\left(\frac{1}{2}\tau\right)\right\} \\
& \times J_0\left(\frac{1}{2}\sqrt{(t-\tau)^2 - (2\ln 2 - \ln x)^2}\right) \\
& \times H(t-\tau - 2\ln 2 + \ln x)\,d\tau \\
& +\frac{1}{4}\int_0^\infty\left\{1 + J_0\left(\frac{1}{2}\tau\right)\right\}J_0\left(\frac{1}{2}\sqrt{(t-\tau)^2 - (\ln x)^2}\right) \\
& \times H(t-\tau - \ln x)\,d\tau\Bigg]
\end{aligned}
\tag{64}
$$

Appendix B: Gaussian and Ricker pulse definitions

The Gaussian pulse load is defined as:

$$
p(t) = -10\exp\left[-\frac{(t-0.15)^2}{0.0004}\right],
\tag{65}
$$

whereas the (modified) Ricker pulse is defined by:

$$p(t) = \frac{\left(0.25u^2 - 0.5\right) e^{-0.25u^2} - 13e^{-13.5}}{0.5 + 13e^{-13.5}}$$

$$\text{with } 0 \leq t \leq \frac{6\sqrt{6}}{\omega_r}, \tag{66}$$

where

$$u = \omega_r t - 3\sqrt{6}, \tag{67}$$

with ω_r denoting the characteristic central circular frequency of the Ricker pulse.

References

1. Mindlin, R.D., Bleich, H.H.: Response of an elastic cylindrical shell to a transverse, step shock wave. ASME J. Appl. Mech. **20**, 189–195 (1953)
2. Schmidt, F.: A new approach to coupled interior-exterior Helmholtz-type problems: theory and applications. Habilitation Thesis, Konrad-Zuse-Zentrum Berlin, Fachbereich Mathematik und Informatik, FU Berlin (2001)
3. Schmidt, F., Hohage, T., Klose, R., Schadle, A., Zschiedrich, L.: Pole condition: a numerical method for Helmholtz-type scattering problem with inhomogeneous exterior domain. J. Comput. Appl. Math. **218**, 61–69 (2008)
4. Zschiedrich, L., Klose, R., Schadle, A., Schmidt, F.: A new finite element realization of the perfectly matched layer method for Helmholtz scattering problems on polygonal domains in two dimensions. J. Comput. Appl. Math. **188**, 12–32 (2006)
5. Givoli, D., Keller, J.B.: A finite element method for large domains. Comput. Methods Appl. Mech. Eng. **76**, 41–66 (1989)
6. Givoli, D., Keller, J.B.: Non-reflecting boundary conditions for elastic waves. Wave Motion **12**(3), 261–279 (1990)
7. Engquist, B., Majda, A.: Absorbing boundary conditions for the numerical simulation of waves. Math. Comput. **31**(139), 629–651 (1977)
8. Bayliss, A., Turkel, E.: Radiation boundary conditions for wave-like equations. Commun. Pure Appl. Math. **33**, 707–725 (1980)
9. Higdon, R.L.: Absorbing boundary conditions for elastic waves. Geophysics **56**(2), 231–241 (1991)
10. Givoli, D., Neta, B.: High-order non-reflecting boundary scheme for time-dependent waves. J. Comput. Phys. **186**(1), 24–46 (2003)
11. Kallivokas, L.F., Lee, S.: Local absorbing boundaries of elliptical shape for scalar waves. Comput. Methods Appl. Mech. Eng. **193**, 4979–5015 (2004)
12. Bérenger, J.-P.: A perfectly matched layer for the absorption of electromagnetic waves. J. Comput. Phys. **114**(2), 185–200 (1994)
13. Chew, W.C., Weedon, W.H.: A 3D perfectly matched medium from modified Maxwell's equations with stretched coordinates. Microw. Opt. Technol. Lett. **7**(13), 599–604 (1994)
14. Hu, F.Q.: On absorbing boundary conditions for linearized Euler equations by a perfectly matched layer. J. Comput. Phys. **129**, 201–219 (1996)
15. Hesthaven, J.S.: On the analysis and construction of perfectly matched layers for the linearized Euler equations. J. Comput. Phys. **142**, 129–147 (1998)
16. Harari, I., Slavutin, M., Turkel, E.: Analytical and numerical studies of a finite element PML for the helmholtz equation. J. Comput. Acoust. **8**(1), 121–137 (2000)
17. Harari, I., Albocher, U.: Studies of FE/PML for exterior problems of time-harmonic elastic waves. Comput. Methods Appl. Mech. Eng. **195**, 3854–3879 (2006)
18. Turkel, E., Yefet, A.: Absorbing PML boundary layers for wave-like equations. Appl. Numer. Math. **27**, 533–557 (1998)
19. Israeli, M., Orszag, S.: Approximation of radiation boundary conditions. J. Comput. Phys. **41**, 115–135 (1981)
20. Qi, Q., Geers, T.L.: Evaluation of the perfectly matched layer for computational acoustics. J. Comput. Phys. **139**(1), 166–183 (1998)
21. Zeng, Y.Q., He, J.Q., Liu, Q.H.: The application of the perfectly matched layer in numerical modeling of wave propagation in poroelastic media. Geophysics **66**(4), 1258–1266 (2001)
22. Chew, W.C., Liu, Q.H.: Perfectly matched layers for elastodynamics: a new absorbing boundary condition. J. Comput. Acoust. **4**(4), 341–359 (1996)
23. Hastings, F.D., Schneider, J.B., Broschat, S.L.: Application of the perfectly matched layer (PML) absorbing boundary condition to elastic wave propagation. J. Acoust. Soc. Am. **100**(5), 3061–3069 (1996)
24. Liu, Q.H.: Perfectly matched layers for elastic waves in cylindrical and spherical coordinates. J. Acoust. Soc. Am. **105**(4), 2075–2084 (1999)
25. Collino, F., Monk, P.: The perfectly matched layer in curvilinear coordinates. SIAM J. Sci. Comput. **19**(6), 2061–2090 (1998)
26. Collino, F., Tsogka, C.: Application of the perfectly matched absorbing layer model to the linear elastodynamic problem in anisotropic heterogeneous media. Geophysics **66**(1), 294–307 (2001)
27. Zheng, Y., Huang, X.: Anisotropic perfectly matched layers for elastic waves in cartesian and curvilinear coordinates. Earth Research Laboratory Report, Massachusetts Institute of Technology, Cambridge (2002)
28. Abarbanel, S., Gottlieb, D.: A mathematical analysis of the PML method. J. Comput. Phys. **134**, 357–363 (1997)
29. Becache, E., Fauqueux, S., Joly, P.: Stability of perfectly matched layers, group velocities and anisotropic waves. J. Comput. Phys. **188**, 399–433 (2003)
30. Becache, E., Petropoulos, P.G., Gedney, S.D.: On the long-time behavior of unsplit perfectly matched layers. IEEE Trans. Antennas Propag. **52**(5), 1335–1342 (2004)
31. Komatitsch, D., Tromp, J.: A perfectly matched layer absorbing boundary condition for the second-order seismic wave equation. Geophys. J. Int. **154**, 146–153 (2003)
32. Basu, U., Chopra, A.K.: Perfectly matched layers for transient elastodynamics of unbounded domains. Int. J. Numer. Methods Eng. **59**, 1039–1074 (2004)
33. Basu, U., Chopra, A.K.: Perfectly matched layers for time-harmonic elastodynamics of unbounded domains: theory and finite-element implementation. Comput. Methods Appl. Mech. Eng. **192**, 1337–1375 (2003)
34. Oden, J.T., Reddy, J.N.: On mixed finite element approximations. SIAM J. Numer. Anal. **13**(3), 393–404 (1976)
35. Sheu, M.-G.: On theories and applications of mixed finite element methods for linear boundary-value problems. Comput. Math. Appl. **4**(4), 333–347 (1978)

36. Brezzi, F., Bathe, K.J.: A discourse on the stability conditions for mixed finite element formulations. Comput. Methods Appl. Mech. Eng. **82**, 27–57 (1990)

37. Carey, G.F., Oden, J.T.: Finite Elements—A Second Course, vol. II. Prentice Hall, Englewood Cliffs (1983)

38. Brezzi, F., Fortin, M.: Mixed And Hybrid Finite Element Methods. Springer, New York (1991)

39. Arnold, D. N.: Mixed finite element methods for elliptic problems. Comput. Methods Appl. Mech. Eng. **82**, 281–300 (1990)

40. Brezzi, F.: A survey of mixed finite element method. In: Dwoyer, D., Hussaini, M., Voigt, R. (eds.) Finite Elements Theory and Application, pp. 34–49. Springer, New York (1988)

41. Raviart, P.A., Thomas, J.M.: A mixed finite element method for second order elliptic problems. In: Galligani, I., Magenes, E. (eds.) Mathematical Aspects of the Finite Element Method. Lecture Notes in Mathematics, vol. 606, pp. 292–315. Springer, New York (1977)

42. Johnson, C., Mercier, B.: Some equilibrium finite element methods for two-dimensional elasticity problems. Numer. Math. **30**, 103–116 (1978)

43. Brezzi, F., Douglas, J., Marini, L.D.: Two families of mixed finite element methods for second order elliptic problems. Numer. Math. **47**, 217–235 (1985)

44. Arnold, D.N., Brezzi, F., Fortin, M.: A stable finite element for the Stokes equations. Calcolo **21**, 337–344 (1984)

45. Arnold, D.N., Brezzi, F., Douglas, J.: PEERS: a new mixed finite element for plane elasticity. Jpn. J. Appl. Math. **1**, 347–367 (1984)

46. Nédélec, J.C.: Mixed finite elements in R^3. Numer. Math. **35**, 315–341 (1980)

47. Arnold, D.N., Douglas, J., Gupta, C.P.: A family of higher order mixed finite element methods for plane elasticity. Numer. Math. **45**, 1–22 (1984)

48. Marini, L.D.: An inexpensive method for the evaluation of the solution of the lowest order raviart-thomas mixed method. SIAM J. Numer. Anal. **22**(3), 493–496 (1985)

49. Nédélec, J.C.: A new family of mixed finite elements in R^3. Numer. Math. **50**, 57–81 (1986)

50. Arnold, D.N., Falk, R.S.: A new mixed formulation for elasticity. Numer. Math. **53**, 13–30 (1988)

51. Stenberg, R.: A family of mixed finite elements for the elasticity problem. Numer. Math. **53**, 513–538 (1988)

52. Frasca, L.P., Hughes, T.J.R., Loula, A.F.D., Miranda, I.: A new family of stable elements for nearly incompressible elasticity based on a mixed Petrov-Galerkin finite element formulation. Numer. Math. **53**, 123–141 (1988)

53. Morley, M.E.: A family of mixed finite elements for linear elasticity. Numer. Math. **55**, 633–666 (1989)

54. Brezzi, F., Marini, D.: A survey on mixed finite element approximations. IEEE Trans. Magn. **30**(5), 3547–3551 (1994)

55. Bécache, E., Joly, P., Tsogka, C.: An analysis of new mixed finite elements for the approximation of wave propagation problems. SIAM J. Numer. Anal. **37**(4), 1053–1084 (2000)

56. Arnold, D.N., Winther, R.: Mixed finite elements for elasticity. Numer. Math. **92**, 401–419 (2002)

57. Bécache, E., Joly, P., Tsogka, C.: A new family of mixed finite elements for the linear elastodynamic problem. SIAM J. Numer. Anal. **39**(6), 2109–2132 (2002)

58. Arnold, D.N., Winther, R.: Mixed finite elements for elasticity in the stress-displacement formulation. In: Chen, Z., Glowinski, R., Li, K. (eds.) Current Trends in Scientific Computing, Contemporary Mathematics, vol. 329, pp. 33–42 (2003)

59. Arnold, D.N., Awanou, G.: Rectangular mixed finite elements for elasticity. Math. Models Methods Appl. Sci. **15**(9), 1417–1429 (2005)

60. Chen, Z.: Finite Element Methods and Their Applications, 1st edn. Springer, New York (2005)

61. Arnold, D.N., Falk, R.S., Winther, R.: Mixed finite element methods for linear elasticity with weakly imposed symmetry. Math. Comput. **76**(260), 1699–1723 (2005)

62. Festa, G., Vilotte, J.-P.: The Newmark scheme as velocity-stress time-staggering: an efficient PML implementation for spectral element simulations of elastodynamics. Geophys. J. Int. **161**, 789–812 (2005)

63. Cohen, G., Fauqueux, S.: Mixed spectral finite elements for the linear elasticity system in unbounded domains. SIAM J. Sci. Comput. **26**(3), 864–884 (2005)

64. Chen, J., Chen, Z.: An adaptive perfectly matched layer technique for 3-D time-harmonic electromagnetic scattering problems. Math. Comput. **77**(262), 673–698 (2008)